Modeling size effects in microwire torsion: A comparison between a Lagrange multiplier-based and a CurlF$^{\mathrm{p}}$ gradient crystal plasticity model

Vikram Phalke[a,b], Tobias Kaiser[c], Jean–Michel Scherer[d,a], Samuel Forest[a]

[a] *MINES ParisTech, PSL University, MAT – Centre des matériaux, CNRS UMR 7633, BP 87 91003 Evry, France*
[b] *Safran Tech, Rue des Jeunes Bois, Châteaufort, 78772, Magny-Les-Hameaux, France*
[c] *Institute of Mechanics, Department of Mechanical Engineering, TU Dortmund University, Leonhard-Euler-Str. 5, Dortmund D-44227, Germany*
[d] *Université Paris-Saclay, CEA, Service d'Etude des Matériaux Irradiés, 91191, Gif-sur-Yvette, France*

Abstract

The size-dependent response of metallic microwires under monotonic and cyclic torsion is modeled using a reduced-order strain gradient crystal plasticity approach involving a single scalar-valued micromorphic variable. It is compared with the response predicted by the $CurlF^p$ model proposed in (Kaiser and Menzel, 2019a), which is based on the complete dislocation density tensor. It is shown that in cyclic non-uniform plastic deformation processes, the gradient of the scalar-valued internal variable in the reduced-order model predicts isotropic hardening in contrast to kinematic-type hardening produced by the $CurlF^p$ model due to a dislocation-induced back-stress component. The arising size effect in the monotonic torsion tests is described by the normalized torque T/R^3 as a function of the ratio of the radius of the microwire R and characteristic length scale ℓ. In the size-dependent domain, characterized by an inflection point on the corresponding curve, the scaling law $T/R^3 \sim (R/\ell)^n$ can be identified, and explicit relations are found for the power n. The relative evolution of SSD and GND densities during torsion is described in detail.

Keywords: Gradient crystal plasticity; Reduced-order model; $CurlF^p$ model; Microwire torsion tests; Size effect; Scaling law; Micromorphic crystal plasticity

Contents

1 Introduction **2**

2 Constitutive framework **5**

2.1 Kinematics 5

2.2 Rate-dependent crystal plasticity model 5

3 Reduced-order gradient crystal plasticity theory **6**

3.1 Micromorphic model 6

3.2 Lagrange multiplier-based model 8

3.3 Dislocation density-based hardening 9

4 $CurlF^p$ gradient crystal plasticity theory **10**
4.1 $CurlF^p$ model . . . 10
4.2 Equivalence of higher-order modulus A and material parameter H_D in single-slip . . . 13

5 Application to microwire torsion tests **15**
5.1 Problem setup . . . 16
5.2 Identification of material parameters . . . 16
5.3 Results and discussion . . . 18
5.3.1 Comparison of predicted size effects . . . 18
5.3.2 Scaling law . . . 24

6 Conclusion **25**

A Summary of constitutive equations in reduced-order and $CurlF^p$ models **27**

1. Introduction

In classical continuum crystal plasticity models, the hardening behavior can be described by incorporating the internal variables related to scalar dislocation densities (McDowell, 2008). There are mainly two types of dislocation families to be considered. The dislocations generated during the plastic deformation through random trapping with each other are called Statistically Stored Dislocations (SSDs). On the other hand, Geometrically Necessary Dislocations (GNDs) are required for the compatible deformation of the crystal under inhomogeneous plastic deformation processes (Ashby, 1970). In classical continuum crystal plasticity models, the contribution of SSD density ρ_S to strain hardening is considered to be dominant compared to the GND density, ρ_G. These classical SSD-based crystal plasticity models do not usually feature a characteristic length scale and hence cannot predict experimentally observed size effects documented in (Fleck and Hutchinson, 1993; Fleck et al., 1994; Gao et al., 1999; Stölken and Evans, 1998). The gradient of shear strain is associated with the storage of GNDs. The GNDs control the material strain hardening along with SSDs, and accounting for the latter in the model formulation naturally gives rise to a characteristic length scale according to (Ashby, 1970; Acharya and Bassani, 2000; Gurtin, 2002; Cordero et al., 2012).

The GNDs are associated with the incompatible part of plastic deformations and can be quantified in terms of the dislocation density tensor (Nye, 1953; Bilby et al., 1955).The introduction of complete dislocation density tensor into the constitutive framework intrinsically gives rise to latent kinematic hardening (Steinmann, 1996; Bayley et al., 2006). Moreover, the introduction of the dislocation density tensor in the free energy density function is motivated on physical grounds as opposed to purely phenomenological modeling approaches (Wulfinghoff et al., 2015; Kaiser and Menzel, 2019b,a).

The micromorphic theory described in (Eringen, 1999) relies on the introduction of a non-symmetric second-order tensor of microdeformation as the additional degree of freedom accounting

for the rotation and distortion of a triad of directors attached to the microstructure. The micromorphic approach has been extended to other types of mechanical variables, including plastic strain and damage variables by Forest (2009, 2016). It was used to investigate strain localization phenomena by Dillard et al. (2006); Anand et al. (2012); Mazière and Forest (2015); Brepols et al. (2017) and to predict size effects in crystal plasticity by Cordero et al. (2010); Aslan et al. (2011); Wulfinghoff et al. (2013); Ling et al. (2018); Scherer et al. (2019, 2020); Ryś et al. (2020). In contrast to Eringen's original micromorphic theory, the reduced-order micromorphic theory relies on a single scalar-valued additional degree of freedom at each material point, akin to accumulated plastic strain or slip (Wulfinghoff and Böhlke, 2012; Wulfinghoff et al., 2013; Erdle and Böhlke, 2017; Ling et al., 2018; Scherer et al., 2019). The reduced-order micromorphic crystal plasticity theory introduces a scalar microslip variable related to accumulated plastic slip and its gradient as the arguments of the free energy density function. The quasi-equality between the microslip variable and accumulated plastic slip is ensured by the coupling modulus H_χ, playing the role of a penalty parameter. Usually, a high value of the coupling modulus H_χ ensures that the microslip variable and accumulated plastic slip almost coincide. This micromorphic model with high values of the coupling modulus can be interpreted as a numerical method to implement a gradient plasticity model; see for instance (Anand et al., 2012). Numerical difficulties associated with penalty methods can be overcome using the Lagrange multiplier-based model introduced by Zhang et al. (2018) and Scherer et al. (2020). The latter makes use of a Lagrange multiplier λ, a nodal degree of freedom in addition to the micromorphic one, in order to enforce equality between microslip variable and accumulated plastic slip (Scherer et al., 2020).

Gradient plasticity and micromorphic models involving the gradient or rotational part of the plastic deformation tensor generally require a large number of additional internal variables and nodal degrees of freedom leading to a significant increase in the computational cost. For instance, the full-order microcurl model proposed by Cordero et al. (2010) and the gradient plasticity model by Panteghini and Bardella (2018) require at least 9 (3D) and 12 (2D) additional nodal degrees of freedom. The complexity in the numerical implementation further increases the computational modeling efforts. The differences in the formulation of various gradient plasticity theories result in distinct and sometimes non-physical responses, which raises the necessity of comparing different gradient plasticity models (Peerlings et al., 2001). A comparison between five gradient-enhanced phenomenological approaches in a continuum damage setting can be found in (Geers et al., 2000), and between implicit and explicit gradient formulations in (Peerlings et al., 2001). The computational advantages of a gradient plasticity formulation including the equivalent plastic strain as an additional degree of freedom are investigated in (Wulfinghoff and Böhlke, 2012). Moreover, the gradient crystal plasticity theory proposed by Gurtin (2002) is used in (Bittencourt et al., 2003) to explore to which extent the results from the discrete dislocation simulations can be reproduced. It is found that the gradient plasticity reproduces the behavior seen in the discrete dislocation simulations in remarkable detail. However, only a few studies are dedicated to the comparison between various gradient crystal plasticity approaches and the determination of the advantages and drawbacks of the many existing theories. For instance, the

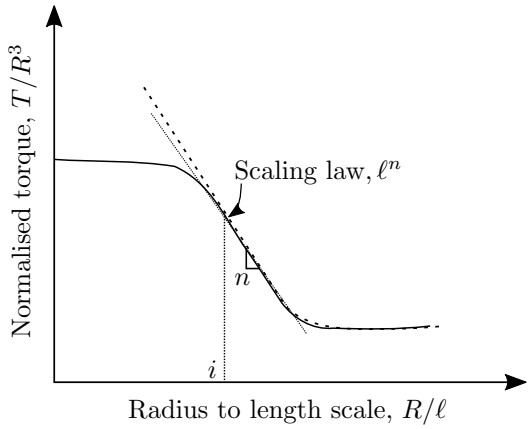

Fig. 1: Schematic log-log plot characterizing the effect of the ratio of the microwire radius R to the characteristic length scale ℓ on the normalized torque T/R^3: size effect with bounded (solid line) and unbounded (dashed line) asymptotic regimes, power law in the transition domain (dotted line), n is the slope of the size dependent domain and i is the inflection point of the curve.

detailed comparison of the micropolar crystal plasticity model (Mayeur et al., 2011) and the gradient crystal plasticity model proposed by Gurtin (2002) can be found in (Mayeur and McDowell, 2014).

It is therefore the objective of this work to compare a computationally efficient Lagrange multiplier-based model that involves a single scalar-valued variable with the $CurlF^p$ model proposed in (Kaiser and Menzel, 2019a) for monotonic and cyclic microwire torsion tests. All models and simulations are presented and performed within the finite deformation framework. The scaling law $T/R^3 \propto (R/\ell)^n$ for the microwire torsion tests, which characterizes the effect of the ratio of the radius of the microwire R and characteristic length scale ℓ on the normalized torque T/R^3 using both reduced-order micromorphic and Lagrange multiplier-based models is obtained. Such scaling laws were derived for the periodic shearing of a laminate at small strains and small rotations in (Cordero et al., 2010; Ryś et al., 2020). Fig. 1 shows schematically the effect of R/ℓ on the normalized torque T/R^3, which is found in the present work. The main features of the diagram are the inflection point i and the slope n of the size-dependent domain. For small values of R/ℓ, a bounded (for the micromorphic model), or an unbounded (for the Lagrange multiplier-based model), asymptotic behavior can be obtained. At large values of R/ℓ, the observed asymptotic behavior corresponds to the size-independent response of classical crystal plasticity models. More details will also be given regarding the evolution of the fields of plastic strain, SSD and GND densities during torsion.

The outline of the paper is as follows: In section 2, the constitutive framework for rate-dependent crystal plasticity is presented. The main features of the reduced-order micromorphic and the Lagrange multiplier-based models are presented in section 3. In section 4, the constitutive framework of the $CurlF^p$ model and the equivalence between the higher-order modulus A from the Lagrange multiplier-based model and the material parameter H_D from the $CurlF^p$ model are demonstrated in the single-slip problem. Section 5 is dedicated to the simulation of representative boundary-value problems, and size effects predicted by the Lagrange multiplier-based model are compared to the $CurlF^p$ model

predictions for monotonic and cyclic microwire torsion tests. Concluding remarks follow in section 6.

The following notations are used in this contribution: Underlined $\underline{\boldsymbol{A}}$ and under-waved bold $\underset{\sim}{\boldsymbol{A}}$ characters are used to denote first-order and second-order tensors, respectively. The transpose, inverse and time derivative are denoted by $\underset{\sim}{\boldsymbol{A}}^T$, $\underset{\sim}{\boldsymbol{A}}^{-1}$ and $\dot{\underset{\sim}{\boldsymbol{A}}}$. Simple and double contractions are understood in the sense $\underline{\boldsymbol{a}} \cdot \underline{\boldsymbol{b}} = a_i b_j$ and $\underset{\sim}{\boldsymbol{A}} : \underset{\sim}{\boldsymbol{B}} = A_{ij} B_{ij}$. Moreover, the following tensor products are used: $\underline{\boldsymbol{a}} \otimes \underline{\boldsymbol{b}} = a_i b_i \underline{\boldsymbol{e}}_j \otimes \underline{\boldsymbol{e}}_j$, $\underset{\sim}{\boldsymbol{A}} \otimes \underset{\sim}{\boldsymbol{B}} = A_{ij} B_{kl} \underline{\boldsymbol{e}}_i \otimes \underline{\boldsymbol{e}}_j \otimes \underline{\boldsymbol{e}}_k \otimes \underline{\boldsymbol{e}}_l$, $\underset{\sim}{\boldsymbol{A}} \underline{\otimes} \underset{\sim}{\boldsymbol{B}} = A_{ik} B_{jl} \underline{\boldsymbol{e}}_i \otimes \underline{\boldsymbol{e}}_j \otimes \underline{\boldsymbol{e}}_k \otimes \underline{\boldsymbol{e}}_l$ and $\underset{\sim}{\boldsymbol{A}} \overline{\otimes} \underset{\sim}{\boldsymbol{B}} = A_{il} B_{jk} \underline{\boldsymbol{e}}_i \otimes \underline{\boldsymbol{e}}_j \otimes \underline{\boldsymbol{e}}_k \otimes \underline{\boldsymbol{e}}_l$. The curl of a second-order tensor $\underset{\sim}{\boldsymbol{A}}$ with respect to the reference configuration is defined as $(\mathrm{Curl} \underset{\sim}{\boldsymbol{A}})_{ij} = \epsilon_{ipq} A_{jq,p} \underline{\boldsymbol{e}}_i \otimes \underline{\boldsymbol{e}}_j$, with ϵ_{ipq} denoting the coefficients of the permutation tensor. Similarly, the spin operator which relates the axial vector to the corresponding skew-symmetric second-order tensor in the reference configuration is defined as $(\mathrm{Spin}\, \underline{\boldsymbol{N}})_{ij} = -\epsilon_{ijq} N_q \underline{\boldsymbol{e}}_i \otimes \underline{\boldsymbol{e}}_j$.

2. Constitutive framework

2.1. Kinematics

A finite deformation framework is used throughout the work, which is based on the multiplicative decomposition of the total deformation gradient $\underset{\sim}{\boldsymbol{F}}$ into an elastic part $\underset{\sim}{\boldsymbol{F}}^e$ and a plastic part $\underset{\sim}{\boldsymbol{F}}^p$, i.e. $\underset{\sim}{\boldsymbol{F}} = \underset{\sim}{\boldsymbol{F}}^e \cdot \underset{\sim}{\boldsymbol{F}}^p$ (see, e.g., Lee and Liu (1967); Willis (1969); Rice (1971); Mandel (1973); Teodosiu and Sidoroff (1976)). The volumetric mass densities with respect to the reference, the intermediate and the current configuration are ρ_0, $\rho_\#$ and ρ, respectively, and expressed as

$$J = \det(\underset{\sim}{\boldsymbol{F}}) = \frac{\rho_0}{\rho}, \quad J^e = \det(\underset{\sim}{\boldsymbol{F}}^e) = \frac{\rho_\#}{\rho}, \quad J^p = \det(\underset{\sim}{\boldsymbol{F}}^p) = \frac{\rho_0}{\rho_\#}. \tag{1}$$

Moreover, it is assumed that the plastic flow is incompressible such that

$$J^p = \det \underset{\sim}{\boldsymbol{F}}^p = 1, \quad J^e = J = \det \underset{\sim}{\boldsymbol{F}}. \tag{2}$$

The multiplicative decomposition of $\underset{\sim}{\boldsymbol{F}}$ leads to the partition of the spatial velocity gradient $\underset{\sim}{\boldsymbol{L}}$ into an elastic part $\underset{\sim}{\boldsymbol{L}}^e$ and a plastic part $\underset{\sim}{\boldsymbol{L}}^p$ as follows:

$$\underset{\sim}{\boldsymbol{L}} = \dot{\underset{\sim}{\boldsymbol{F}}} \cdot \underset{\sim}{\boldsymbol{F}}^{-1} = \dot{\underset{\sim}{\boldsymbol{F}}}^e \cdot \underset{\sim}{\boldsymbol{F}}^{e-1} + \underset{\sim}{\boldsymbol{F}}^e \cdot \dot{\underset{\sim}{\boldsymbol{F}}}^p \cdot \underset{\sim}{\boldsymbol{F}}^{p-1} \cdot \underset{\sim}{\boldsymbol{F}}^{e-1} = \underset{\sim}{\boldsymbol{L}}^e + \underset{\sim}{\boldsymbol{L}}^p. \tag{3}$$

The elastic Green–Lagrange strain tensor $\underset{\sim}{\boldsymbol{E}}^e_{GL}$ is introduced as

$$\underset{\sim}{\boldsymbol{E}}^e_{GL} = \frac{1}{2}(\underset{\sim}{\boldsymbol{F}}^{eT} \cdot \underset{\sim}{\boldsymbol{F}}^e - \underset{\sim}{\boldsymbol{1}}), \tag{4}$$

with $\underset{\sim}{\boldsymbol{1}}$ denoting the second-order identity tensor.

2.2. Rate-dependent crystal plasticity model

Most rate-independent crystal plasticity theories lead to an ill-conditioned problem regarding the selection of active slip systems and the increments of shear on the active slip systems as emphasized in (Anand and Kothari, 1996; Miehe et al., 1999; Busso and Cailletaud, 2005). One way to overcome this difficulty is to work within a rate-dependent framework. Here, a rate-dependent overstress-type

flow rule is adopted to facilitate the determination of the set of active slip systems. It is based on a Schmid-type yield function defined as

$$f^r = |\tau^r| - \tau_c^r, \tag{5}$$

involving the resolved shear stress τ^r on the slip system r, which is the driving force to trigger plastic slip, and the corresponding critical resolved shear stress τ_c^r. The resolved shear stress τ^r on slip system r is defined as

$$\tau^r = \underset{\sim}{\boldsymbol{\Pi}}^M : (\underline{\boldsymbol{m}}^r \otimes \underline{\boldsymbol{n}}^r), \quad \text{with} \quad \underset{\sim}{\boldsymbol{\Pi}}^M = J^e \underset{\sim}{\boldsymbol{F}}^{eT} \cdot \underset{\sim}{\boldsymbol{\sigma}} \cdot \underset{\sim}{\boldsymbol{F}}^{-eT}, \tag{6}$$

where $\underset{\sim}{\boldsymbol{\Pi}}^M$ is the Mandel stress tensor defined with respect to the intermediate configuration, $\underline{\boldsymbol{m}}^r$ is the slip direction, $\underline{\boldsymbol{n}}^r$ is the slip normal and $\underset{\sim}{\boldsymbol{\sigma}}$ is the Cauchy stress tensor. The shear strain rate $\dot{\gamma}^r$ on each slip system r is then given by the following rate-dependent flow rule

$$\dot{\gamma}^r = \dot{\gamma}_0 \left\langle \frac{f^r}{\tau_0} \right\rangle^m \operatorname{sign}(\tau^r), \tag{7}$$

with Macauley brackets $< \bullet >$ denoting the positive part of $\bullet$, $\dot{\gamma}_0$ is the reference strain rate and m is a material parameter controlling the rate sensitivity of the material response– i.e. high values of $\dot{\gamma}_0$ and m result in a low rate-sensitivity. Moreover, τ_0 is the initial critical resolved shear stress.

Furthermore, the plastic deformation rate is the result of slip processes on N distinct slip systems, i.e.

$$\dot{\underset{\sim}{\boldsymbol{F}}}^p \cdot \underset{\sim}{\boldsymbol{F}}^{p-1} = \sum_{r=1}^{N} \dot{\gamma}^r (\underline{\boldsymbol{m}}^r \otimes \underline{\boldsymbol{n}}^r). \tag{8}$$

3. Reduced-order gradient crystal plasticity theory

3.1. Micromorphic model

According to the micromorphic approach, the variables carrying the targeted gradient effects are selected from the available state variables. They can be tensors of any rank (Forest, 2016). The model is called reduced-order micromorphic when the micromorphic variable is a scalar quantity, as done in the model proposed by Ling et al. (2018) which is summarized in this section.

The material points are defined by the position vector $\underline{\boldsymbol{X}}$ in the reference configuration Ω^0 and the position vector $\underline{\boldsymbol{x}}$ in the current configuration Ω^t. They possess two types of degrees of freedom: the displacement vector $\underline{\boldsymbol{u}}(\underline{\boldsymbol{X}}, t) = \underline{\boldsymbol{x}} - \underline{\boldsymbol{X}}$ and the micromorphic scalar microslip variable $\gamma_\chi(\underline{\boldsymbol{X}}, t)$. The associated scalar internal variable is the cumulative plastic strain γ_{cum} introduced as

$$\gamma_{cum} = \int_0^t \sum_{r=1}^{N} |\dot{\gamma}^r| dt. \tag{9}$$

In the present formulation, the set of degrees of freedom (DOF) is, therefore

$$\text{DOF} = \{\underline{\boldsymbol{u}}, \gamma_\chi\}. \tag{10}$$

The gradients of the degrees of freedom with respect to the reference configuration are

$$\underset{\sim}{\boldsymbol{H}} = \frac{\partial \underline{\boldsymbol{u}}}{\partial \underline{\boldsymbol{X}}} = \operatorname{Grad} \underline{\boldsymbol{u}}, \quad \underline{\boldsymbol{K}} = \frac{\partial \gamma_\chi}{\partial \underline{\boldsymbol{X}}} = \operatorname{Grad} \gamma_\chi. \tag{11}$$

The static balance equations and Neumann boundary conditions expressed with respect to the reference configuration are as follows:

$$\operatorname{Div} \underset{\sim}{\boldsymbol{P}} = 0 \quad \text{and} \quad \operatorname{Div} \underline{\boldsymbol{M}} - S = 0, \quad \forall\, \underline{\boldsymbol{X}} \subset \Omega^0, \tag{12}$$

$$\underline{\boldsymbol{T}} = \underset{\sim}{\boldsymbol{P}} \cdot \underline{\boldsymbol{N}} \quad \text{and} \quad M = \underline{\boldsymbol{M}} \cdot \underline{\boldsymbol{N}}, \quad \forall\, \underline{\boldsymbol{X}} \subset \partial\Omega^0, \tag{13}$$

with $\underset{\sim}{\boldsymbol{P}}$ being the Boussinesq (first Piola–Kirchhoff) stress tensor related to the Cauchy stress tensor $\underset{\sim}{\boldsymbol{\sigma}}$ by $\underset{\sim}{\boldsymbol{P}} = J\underset{\sim}{\boldsymbol{\sigma}}\underset{\sim}{\boldsymbol{F}}^{-T}$, S and $\underline{\boldsymbol{M}}$ are the generalized stresses, $\underline{\boldsymbol{T}}$ is traction vector, M is the generalized surface traction and $\underline{\boldsymbol{N}}$ the outward unit normal vector at a boundary of the reference body.

The cumulative plastic strain γ_{cum} is related to the microslip variable γ_χ via the relative plastic strain $e(\underline{\boldsymbol{X}}, t)$ as

$$e(\underline{\boldsymbol{X}}, t) := \gamma_{cum} - \gamma_\chi. \tag{14}$$

The material under consideration is assumed to be characterized by the Helmholtz free energy density function of the following arguments

$$\Psi = \tilde{\Psi}(\underset{\sim}{\boldsymbol{E}}^e_{GL}, e, \underline{\boldsymbol{K}}, \alpha), \tag{15}$$

in terms of the elastic Green-Lagrange strain tensor $\underset{\sim}{\boldsymbol{E}}^e_{GL}$, the relative plastic strain e, the gradient of the microslip variable $\underline{\boldsymbol{K}}$ and the internal hardening variable α. The Helmholtz free energy density function is taken partly as a quadratic potential in the form:

$$\rho_0\tilde{\Psi}(\underset{\sim}{\boldsymbol{E}}^e_{GL}, e, \underline{\boldsymbol{K}}, \alpha) = \frac{1}{2}J^p\underset{\sim}{\boldsymbol{E}}^e_{GL} : \underset{\approx}{\boldsymbol{\Lambda}} : \underset{\sim}{\boldsymbol{E}}^e_{GL} + \frac{1}{2}H_\chi e^2 + \frac{1}{2}\underline{\boldsymbol{K}} \cdot \underset{\sim}{\boldsymbol{A}} \cdot \underline{\boldsymbol{K}} + \rho_0\tilde{\Psi}^p(\alpha), \tag{16}$$

where $\underset{\approx}{\boldsymbol{\Lambda}}$ is the fourth-order tensor of elastic moduli. In the micromorphic approach, two additional material parameters are introduced, namely the coupling modulus H_χ and the higher-order micromorphic stiffness $\underset{\sim}{\boldsymbol{A}}$.

The Clausius-Duhem inequality takes the form

$$\left(J^p\underset{\sim}{\boldsymbol{\Pi}}^e - \rho_0\frac{\partial\tilde{\Psi}}{\partial\underset{\sim}{\boldsymbol{E}}^e_{GL}}\right) : \dot{\underset{\sim}{\boldsymbol{E}}}^e_{GL} - \left(S + \rho_0\frac{\partial\tilde{\Psi}}{\partial e}\right)\dot{e} + \left(\underline{\boldsymbol{M}} - \rho_0\frac{\partial\tilde{\Psi}}{\partial\underline{\boldsymbol{K}}}\right)\dot{\underline{\boldsymbol{K}}} + J^p\underset{\sim}{\boldsymbol{\Pi}}^M : (\dot{\underset{\sim}{\boldsymbol{F}}}^p \cdot \underset{\sim}{\boldsymbol{F}}^{p-1}) + S\dot{\gamma}_{cum} + X\dot{\alpha} \geq 0, \tag{17}$$

from which the following state laws are adopted:

$$\underset{\sim}{\boldsymbol{\Pi}}^e = \rho_\#\frac{\partial\tilde{\Psi}}{\partial\underset{\sim}{\boldsymbol{E}}^e_{GL}} \quad S = -\rho_0\frac{\partial\tilde{\Psi}}{\partial e} \quad \underline{\boldsymbol{M}} = \rho_0\frac{\partial\tilde{\Psi}}{\partial\underline{\boldsymbol{K}}}, \quad X = -\rho_0\frac{\partial\tilde{\Psi}}{\partial\alpha}, \tag{18}$$

where X is the thermodynamic force associated with internal hardening variable α. The Piola stress tensor with respect to the intermediate configuration is $\underset{\sim}{\boldsymbol{\Pi}}^e = J^e\underset{\sim}{\boldsymbol{F}}^{e-1} \cdot \underset{\sim}{\boldsymbol{\sigma}} \cdot \underset{\sim}{\boldsymbol{F}}^{e-T}$.

Moreover, the specific quadratic form of the potential (16) then leads to the following relations:

$$\underset{\sim}{\boldsymbol{\Pi}}^e = \underset{\approx}{\boldsymbol{\Lambda}} : \underset{\sim}{\boldsymbol{E}}^e_{GL}, \quad S = -H_\chi e = -H_\chi(\gamma_{cum} - \gamma_\chi), \quad \underline{\boldsymbol{M}} = \underset{\sim}{\boldsymbol{A}} \cdot \underline{\boldsymbol{K}}. \tag{19}$$

Additionally, partial differential equation connecting γ_χ and γ_{cum} follows from the previous state laws and the balance equation in (12) as

$$\gamma_\chi - \frac{A}{H_\chi}\triangle_X\,\gamma_\chi = \gamma_{cum}, \tag{20}$$

where $\triangle_X$ stands for the Laplace operator with respect to the reference configuration.

The residual dissipation inequality takes the form

$$D_{res} = J^p \underset{\sim}{\mathbf{\Pi}}^M : (\dot{\underset{\sim}{\boldsymbol{F}}}^p \cdot \underset{\sim}{\boldsymbol{F}}^{p-1}) + S\dot{\gamma}_{cum} + X\dot{\alpha} = \sum_{r=1}^{N} \tau^r \dot{\gamma}^r + S\dot{\gamma}_{cum} + X\dot{\alpha} \geq 0, \tag{21}$$

after consideration of (8) and of plastic incompressibility. The dissipation rate form suggests introducing the following generalized Schmid yield function:

$$f^r = |\tau^r| + S - \tau_c^r = |\tau^r| - (\tau_c^r - S), \quad \text{with} \quad X^r = \tau_c^r, \tag{22}$$

which leads to a yield function of the form

$$f^r = |\tau^r| - (\tau_c^r - S) = |\tau^r| - (\tau_c^r - \operatorname{Div} \underline{\boldsymbol{M}}), \tag{23}$$

once the generalized static balance law (12) is taken into account. In that way, the generalized stress S in the previous equation results in an enhancement of the hardening law and can be regarded as a source of isotropic hardening (or softening). For isotropic and cubic materials, the second-order tensor $\underset{\sim}{\boldsymbol{A}} = A\underset{\sim}{\mathbf{1}}$ involves a single generalized modulus A which is assumed to be constant in space thus leading to the expression of the yield function:

$$f^r = |\tau^r| - (\tau_c^r - A \operatorname{Div}(\operatorname{Grad} \gamma_\chi)) = |\tau^r| - (\tau_c^r - A \triangle_X \gamma_\chi). \tag{24}$$

This generalized yield function is then inserted into the flow rule (7), taking care of the sign of the threshold function, to compute the plastic slip rate of each slip system.

In this work, the micromorphic model is used to derive the scaling laws for the monotonic microwire torsion tests.

3.2. Lagrange multiplier-based model

The Lagrange multiplier-based model was proposed by Fortin and Glowinski (1983) and successfully implemented in (Zhang et al., 2018; Scherer et al., 2020). In this section, the Lagrange multiplier-based model presented in (Scherer et al., 2020) is summarized. The Lagrange multiplier λ is introduced to enforce the strict equality between γ_{cum} and γ_χ in order to transform the previous micromorphic model into a strain gradient crystal plasticity model. It replaces the penalty coefficient represented by the coupling modulus H_χ of the micromorphic model summarized in section 3.1. Therefore, the set of degrees of freedom (DOF) is given by

$$\text{DOF} = \{\underline{\boldsymbol{u}}, \gamma_\chi, \lambda\}. \tag{25}$$

It turns out that the free energy density function in (15) becomes a Lagrangian function L_0. More specifically speaking, the material under consideration is assumed to be characterized by the Lagrangian function $L_0(\underset{\sim}{\boldsymbol{E}}^e_{GL}, e, \underline{\boldsymbol{K}}, \lambda, \alpha)$, in terms of the Green-Lagrange strain tensor $\underset{\sim}{\boldsymbol{E}}^e_{GL}$, the relative plastic strain e, the gradient of the microslip variable $\underline{\boldsymbol{K}}$, the Lagrange multiplier λ, which

is treated as an additional degree of freedom and the internal hardening variable α. The considered form of the Lagrangian function is

$$\rho_0 L_0(\underset{\sim}{\boldsymbol{E}}^e_{GL}, e, \underline{\boldsymbol{K}}, \lambda, \alpha) = \frac{1}{2} J^p \underset{\sim}{\boldsymbol{E}}^e_{GL} : \underset{\approx}{\boldsymbol{\Lambda}} : \underset{\sim}{\boldsymbol{E}}^e_{GL} + \frac{1}{2}\mu_\chi e^2 + \frac{1}{2}\underline{\boldsymbol{K}} \cdot \underset{\sim}{\boldsymbol{A}} \cdot \underline{\boldsymbol{K}} + \lambda e + \rho_0 \tilde{\Psi}^p(\alpha), \tag{26}$$

where μ_χ is a Lagrangian penalty modulus. The Clausius-Duhem inequality then takes the form

$$\left(J^p \underset{\sim}{\boldsymbol{\Pi}}^e - \rho_0 \frac{\partial L_0}{\partial \underset{\sim}{\boldsymbol{E}}^e_{GL}} \right) : \dot{\underset{\sim}{\boldsymbol{E}}}^e_{GL} - \left(S + \rho_0 \frac{\partial L_0}{\partial e} \right) \dot{e} + \left(\underline{\boldsymbol{M}} - \rho_0 \frac{\partial L_0}{\partial \underline{\boldsymbol{K}}} \right) \underline{\dot{\boldsymbol{K}}} +$$

$$+ J^p \underset{\sim}{\boldsymbol{\Pi}}^M : (\dot{\underset{\sim}{\boldsymbol{F}}}^p \cdot \underset{\sim}{\boldsymbol{F}}^{p-1}) + S\dot{\gamma}_{cum} + \rho_0 \frac{\partial L_0}{\partial \alpha} \dot{\alpha} \geq 0. \tag{27}$$

This gives rise to the following state laws:

$$\underset{\sim}{\boldsymbol{\Pi}}^e = \rho_\# \frac{\partial L_0}{\partial \underset{\sim}{\boldsymbol{E}}^e_{GL}} \quad S = -\rho_0 \frac{\partial L_0}{\partial e} \quad \underline{\boldsymbol{M}} = \rho_0 \frac{\partial L_0}{\partial \underline{\boldsymbol{K}}}, \quad X = -\rho_0 \frac{\partial L_0}{\partial \alpha}. \tag{28}$$

Furthermore, the specific quadratic form of the Lagrangian (26) then leads to the following relations

$$\underset{\sim}{\boldsymbol{\Pi}}^e = \underset{\approx}{\boldsymbol{\Lambda}} : \underset{\sim}{\boldsymbol{E}}^e_{GL}, \quad S = \lambda - \mu_\chi(\gamma_{cum} - \gamma_\chi), \quad \underline{\boldsymbol{M}} = \underset{\sim}{\boldsymbol{A}} \cdot \underline{\boldsymbol{K}}. \tag{29}$$

The residual dissipation has the same form as (21) and leads to the introduction of the following generalized Schmid yield function:

$$f^r = |\tau^r| + S - \tau^r_c = |\tau^r| - (\tau^r_c - S) = |\tau^r| - (\tau^r_c - \lambda + \mu_\chi(\gamma_{cum} - \gamma_\chi)). \tag{30}$$

Again, this generalized yield function can be inserted into the flow rule (7) to evaluate the plastic slip rate of each slip system. The penalty parameter μ_χ is similar to the micromorphic penalization term H_χ but bears a different meaning. In simulations, the parameter μ_χ can take a much lower value than H_χ and provides additional coercivity.

In the present work, the Lagrange multiplier-based model is used to compare the size effects predicted by the $CurlF^p$ model because the $CurlF^p$ model is a strain gradient plasticity model and thus should be compared more directly to the Lagrange multiplier-based model.

3.3. Dislocation density-based hardening

The strain hardening behavior relies on a dislocation density-based hardening model, which takes dislocation interactions into account. Following the work of Kubin et al. (2008), the rate of the critical resolved shear stress τ^r_c is related to the scalar dislocation densities ϱ^u according to

$$\tau^r_c = \tau_0 + \mu \sqrt{\sum_{u=1}^{N} h^{ru} \varrho^u}, \tag{31}$$

where τ_0 is the initial critical resolved shear stress, μ is the shear modulus and h^{ru} is the interaction matrix describing long-range interaction between dislocations. Moreover, ϱ^u is the non-dimensional dislocation density such that $\varrho^u/b^2 = \rho^u$, with ρ^u as the usual SSD density, i.e. the length of dislocation

lines per unit volume with b denoting the norm of the dislocation Burgers vector $\underline{\boldsymbol{b}}$. The following equation gives the evolution of the dislocation density

$$\dot{\varrho}^r = |\dot{\gamma}^r| \left(\frac{\sqrt{\sum_{u=1}^{N} a^{ru} \varrho^u}}{\kappa} - G_c \varrho^r \right). \tag{32}$$

The first term in the previous equation corresponds to dislocation multiplication, whereas the second term accounts for dislocation annihilation. The dislocation interaction is described by the matrix a^{ru}, κ is a constant material parameter and G_c is the critical distance controlling the annihilation of dislocations with opposite signs. The structure of the matrices h^{ru} and a^{ru} is described in (Ling et al., 2018).

The part of the free energy due to the internal hardening variable is assumed to be of the form (Abrivard et al., 2012):

$$\rho_0 \tilde{\Psi}^p(\alpha^r) = \mu \xi \sum_{r=1}^{N} \frac{1}{2} (\alpha^r)^2, \tag{33}$$

where ξ is a constant approximately equal to 0.3. The dissipation due to the internal hardening variable α^r in (17) on each slip system r involves thermodynamic force given by

$$X^r = -\rho_0 \frac{\partial \tilde{\Psi}^p}{\partial \alpha^r} = -\mu \xi \alpha^r. \tag{34}$$

Moreover, it is assumed that the internal hardening variable α^r depends on the SSDs as follows:

$$\alpha^r = \sqrt{\sum_{u=1}^{N} h^{ru} \varrho^u}. \tag{35}$$

4. $CurlF^p$ gradient crystal plasticity theory

4.1. $CurlF^p$ model

In this section, the gradient plasticity theory based on the complete dislocation density tensor elaborated in (Kaiser and Menzel, 2019b) is briefly summarized. The $CurlF^p$ framework proposed by Kaiser and Menzel (2019b) relies on the interpretation of incompatible plastic deformation processes in terms of the dislocation density tensor. The model formulation is based on introducing the dislocation density tensor as an argument of the free energy density function and assumes an extended non-local form of the dissipation inequality as proposed by Polizzotto and Borino (1998).

The dislocation density tensor (Steinmann and Stein, 1996; Acharya and Bassani, 2000; Cermelli and Gurtin, 2001; Liebe et al., 2003) is defined by

$$\underset{\sim}{\boldsymbol{D}} = \mathrm{Curl}^T(\underset{\sim}{\boldsymbol{F}}^p). \tag{36}$$

The material under consideration is assumed to be characterized by a free energy density function given as

$$\Psi = \tilde{\Psi}(\underset{\sim}{\boldsymbol{F}}, \underset{\sim}{\boldsymbol{F}}^p, \underset{\sim}{\boldsymbol{D}}, \alpha), \tag{37}$$

with α denoting a scalar-valued internal variable, which may be interpreted as a measure of the cumulative plastic strain. Moreover, it is assumed that the gradient-enhanced energy density function is additively decomposed as

$$\rho_0\tilde{\Psi} = \rho_0\tilde{\Psi}^e(\underset{\sim}{\boldsymbol{F}}, \underset{\sim}{\boldsymbol{F}}^p) + \rho_0\tilde{\Psi}^g(\underset{\sim}{\boldsymbol{D}}) + \rho_0\tilde{\Psi}^p(\alpha), \tag{38}$$

where $\tilde{\Psi}^e$, $\tilde{\Psi}^g$ and $\tilde{\Psi}^p$ are the elastic contribution, the energy contribution due to the gradient effect and the energy contribution due to the internal hardening variable, respectively. The energy contribution $\tilde{\Psi}^g$ is expressed as a quadratic function

$$\rho_0\tilde{\Psi}^g(\underset{\sim}{\boldsymbol{D}}) = H_D\underset{\sim}{\boldsymbol{D}} : \underset{\sim}{\boldsymbol{D}}, \tag{39}$$

where H_D is a material parameter proposed in (Kaiser and Menzel, 2019b), which can beinterpreted as a characteristic length scale parameter. The part of the free energy due to the hardening variable α is chosen as

$$\rho_0\tilde{\Psi}^p(\alpha) = \tau_0\alpha + \frac{(\tau_\infty - \tau_0)^2}{H_0}\ln\left(\cosh\left(\frac{H_0\alpha}{\tau_\infty - \tau_0}\right)\right), \tag{40}$$

where the material parameters τ_∞ and H_0 are the saturation strength and the initial hardening rate, respectively. The extended form the dissipation inequality is

$$D_{res} = J^p\underset{\sim}{\boldsymbol{P}} : \dot{\underset{\sim}{\boldsymbol{F}}} - \left(\rho_0\frac{\partial\tilde{\Psi}}{\partial\underset{\sim}{\boldsymbol{F}}} : \dot{\underset{\sim}{\boldsymbol{F}}} + \rho_0\frac{\partial\tilde{\Psi}}{\partial\underset{\sim}{\boldsymbol{F}}^p} : \dot{\underset{\sim}{\boldsymbol{F}}}^p + \rho_0\frac{\partial\tilde{\Psi}}{\partial\underset{\sim}{\boldsymbol{D}}} : \dot{\underset{\sim}{\boldsymbol{D}}} + \rho_0\frac{\partial\tilde{\Psi}}{\partial\alpha} : \dot{\alpha}\right) + \mathcal{P}_0 \geq 0, \tag{41}$$

with $\mathcal{P}_0$ denoting the non-locality residual. The first Piola–Kirchhoff stress tensor is given by

$$\underset{\sim}{\boldsymbol{P}} = \rho_\# \frac{\partial\tilde{\Psi}}{\partial\underset{\sim}{\boldsymbol{F}}}. \tag{42}$$

The reduced form of the dissipation inequality

$$D_{res} = J^p\underset{\sim}{\boldsymbol{\Pi}}^M : (\dot{\underset{\sim}{\boldsymbol{F}}}^p \cdot \underset{\sim}{\boldsymbol{F}}^{p-1}) + \underset{\sim}{\boldsymbol{\Xi}} : \dot{\underset{\sim}{\boldsymbol{D}}} + X\dot{\alpha} + \mathcal{P}_0 \geq 0. \tag{43}$$

The thermodynamic force associated with the internal hardening variable is defined as

$$X = -\rho_0\frac{\partial\tilde{\Psi}^p}{\partial\alpha} = -\left(\tau_0 + (\tau_\infty - \tau_0)\tanh\left(\frac{H_0\alpha}{\tau_\infty - \tau_0}\right)\right), \tag{44}$$

and the energetic dual to the dislocation density tensor is

$$\underset{\sim}{\boldsymbol{\Xi}} = -\rho_0\frac{\partial\tilde{\Psi}}{\partial\underset{\sim}{\boldsymbol{D}}}. \tag{45}$$

Moreover, the evaluation of (45) for the specific form of the energy contribution (39) yields

$$\underset{\sim}{\boldsymbol{\Xi}} = -2H_D\mathrm{Curl}^T(\underset{\sim}{\boldsymbol{F}}^p). \tag{46}$$

By considering an insulation condition $\mathcal{P}_0 = 0$ as in (Kaiser and Menzel, 2019a), the reduced form of the dissipation inequality may be written in terms of

$$D_{res} = J^p\overline{\underset{\sim}{\boldsymbol{M}}} : (\dot{\underset{\sim}{\boldsymbol{F}}}^p \cdot \underset{\sim}{\boldsymbol{F}}^{p-1}) + X\dot{\alpha} \geq 0, \tag{47}$$

giving rise to a balance equation for the generalized stress tensor as

$$J^p \overline{\underset{\sim}{\boldsymbol{M}}} = J^p \underset{\sim}{\boldsymbol{\Pi}}^M + \mathrm{Curl}^T(\underset{\approx}{\boldsymbol{\Xi}}) \cdot \underset{\sim}{\boldsymbol{F}}^{pT}, \quad \text{in} \quad B^0_{dis}. \tag{48}$$

The generalized stress tensor $\overline{\underset{\sim}{\boldsymbol{M}}}$ consists of the Mandel stress tensor $\underset{\sim}{\boldsymbol{\Pi}}^M$ defined in the intermediate configuration and a back-stress term, which is closely related to incompatibilities in the plastic deformation field such that when gradient effects are neglected, $\overline{\underset{\sim}{\boldsymbol{M}}}$ reduces to $\underset{\sim}{\boldsymbol{\Pi}}^M$. The generalized stress tensor is identified as the driving force for plastic deformation processes based on (48). The yield function and the evolution equations are accordingly formulated in terms of the generalized stress tensor. Moreover, the non-ambiguous constitutive boundary condition associated with (48) reads

$$\underset{\approx}{\boldsymbol{\Xi}} \cdot \mathrm{Spn}(\underline{\boldsymbol{N}}) \cdot \underset{\sim}{\boldsymbol{F}}^{pT} = 0, \quad \text{on} \quad \partial B^0_{dis,ext}, \tag{49}$$

where $\underline{\boldsymbol{N}}$ denotes the outward unit normal vector with respect to the considered boundary ∂B^0. The
165 detailed derivation of (48) and (49) can be found in (Kaiser and Menzel, 2019b). The generalized stress tensor in (48) and the constitutive boundary condition in (49) are originally derived on the domain B^0_{dis}, where dissipative processes occur, and on the corresponding external boundary $\partial B^0_{dis,ext}$.

In addition, the relative Mandel stress tensor is introduced as a primary field variable

$$\overline{\underset{\sim}{\boldsymbol{M}}}^{(\mathrm{rel})} = \overline{\underset{\sim}{\boldsymbol{M}}} - \underset{\sim}{\boldsymbol{\Pi}}^M, \tag{50}$$

so that (48) can be written as

$$J^p \overline{\underset{\sim}{\boldsymbol{M}}}^{(\mathrm{rel})} - \mathrm{Curl}^T(\underset{\approx}{\boldsymbol{\Xi}}) \cdot \underset{\sim}{\boldsymbol{F}}^{pT} = 0, \quad \text{in} \quad B^0_{dis}. \tag{51}$$

Substituting (46) in (51) yields the specific form of the relative Mandel stress tensor

$$J^p \overline{\underset{\sim}{\boldsymbol{M}}}^{(\mathrm{rel})} = -2H_D \mathrm{Curl}^T(\mathrm{Curl}^T(\underset{\sim}{\boldsymbol{F}}^p)) \cdot \underset{\sim}{\boldsymbol{F}}^{pT}, \tag{52}$$

which is responsible for the back-stress associated with the kinematic hardening. Additionally, field variable $\underset{\sim}{\boldsymbol{\theta}}^p$ is introduced which is coupled to $\underset{\sim}{\boldsymbol{F}}^p$ in terms of an L_2-projection as follows:

$$0 = \int_{B^0} \eta^{\theta^p} : (\underset{\sim}{\boldsymbol{F}}^p - \underset{\sim}{\boldsymbol{\theta}}^p) dV, \tag{53}$$

where η^{θ^p} is the corresponding test function.

In order to identify the differences between the Lagrange multiplier-based model and the $CurlF^p$ model, the constitutive equations of both models are summarized in Appendix A. Moreover, in the present work, the GND density distribution in monotonic and cyclic loading of microwires using the Lagrange multiplier-based model is calculated from the Euclidean norm of $\mathrm{Curl}^T(\underset{\sim}{\boldsymbol{F}}^p)$. A post-processing technique is used to evaluate the $\mathrm{Curl}^T(\underset{\sim}{\boldsymbol{F}}^p)$ (see also, Busso et al. (2000); Abrivard et al. (2012)). The first step in determining the $\mathrm{Curl}^T(\underset{\sim}{\boldsymbol{F}}^p)$ is to calculate the gradient of $\underset{\sim}{\boldsymbol{F}}^p$ at the integration points. To this end, the known values of $\underset{\sim}{\boldsymbol{F}}^p$ at the integration points are extrapolated to nodes using the shape functions of the elements. The gradients of $\underset{\sim}{\boldsymbol{F}}^p$ at the nodes can next be obtained from the derivatives of the shape functions. Finally, known nodal values of the gradient of $\underset{\sim}{\boldsymbol{F}}^p$ are

interpolated back to the integration points. The Euclidean norm of $\text{Curl}^T(\underset{\sim}{\boldsymbol{F}}^p)$ provides an effective measure of GND density as follows:

$$||\text{Curl}^T(\underset{\sim}{\boldsymbol{F}}^p)|| = b\sum_{r=1}^{N}\rho_G^r, \tag{54}$$

where $||\bullet||$ denotes the Euclidean norm of $\bullet$.

4.2. Equivalence of higher-order modulus A and material parameter H_D in single-slip

The higher-order modulus A from the reduced-order model, refer (24), and material parameter H_D from the $CurlF^p$ theory, refer (46), bear similar physical interpretations. This is demonstrated in this section for a simplified two-dimensional single-slip problem.

A single crystal with a single-slip system is considered. The slip direction $\underline{\boldsymbol{m}}$ and the slip plane normal $\underline{\boldsymbol{n}}$ are

$$\underline{\boldsymbol{m}} = (1,0,0), \quad \underline{\boldsymbol{n}} = (0,1,0). \tag{55}$$

Consider a situation where only one slip system is active. In the absence of lattice distortion and rotation, the plastic part of the deformation gradient $\underset{\sim}{\boldsymbol{F}}^p$ takes the form

$$\underset{\sim}{\boldsymbol{F}}^p = \underset{\sim}{\mathbf{1}} + \gamma\,(\underline{\boldsymbol{m}} \otimes \underline{\boldsymbol{n}}), \tag{56}$$

$$[\underset{\sim}{\boldsymbol{F}}^p]_{ij} = \begin{bmatrix} 1 & \gamma & 0 \\ 0 & 1 & 0 \\ 0 & 0 & 1 \end{bmatrix}. \tag{57}$$

The dislocation density tensor $[\underset{\sim}{\boldsymbol{D}}]_{ij} = [\text{Curl}^T(\underset{\sim}{\boldsymbol{F}}^p)]_{ij}$ is given by

$$[\underset{\sim}{\boldsymbol{D}}]_{ij} = \begin{bmatrix} \frac{\partial F^p_{13}}{\partial X_2} - \frac{\partial F^p_{12}}{\partial X_3} & \frac{\partial F^p_{11}}{\partial X_3} - \frac{\partial F^p_{13}}{\partial X_1} & \frac{\partial F^p_{12}}{\partial X_1} - \frac{\partial F^p_{11}}{\partial X_2} \\ \frac{\partial F^p_{23}}{\partial X_2} - \frac{\partial F^p_{22}}{\partial X_3} & \frac{\partial F^p_{21}}{\partial X_3} - \frac{\partial F^p_{23}}{\partial X_1} & \frac{\partial F^p_{22}}{\partial X_1} - \frac{\partial F^p_{21}}{\partial X_2} \\ \frac{\partial F^p_{33}}{\partial X_2} - \frac{\partial F^p_{32}}{\partial X_3} & \frac{\partial F^p_{31}}{\partial X_3} - \frac{\partial F^p_{33}}{\partial X_1} & \frac{\partial F^p_{32}}{\partial X_1} - \frac{\partial F^p_{31}}{\partial X_2} \end{bmatrix}. \tag{58}$$

Therefore, for the 2-dimensional case and the specific simple shear problem studied,

$$[\underset{\sim}{\boldsymbol{D}}]_{ij} = \begin{bmatrix} 0 & 0 & \frac{\partial \gamma}{\partial X_1} \\ 0 & 0 & 0 \\ 0 & 0 & 0 \end{bmatrix}. \tag{59}$$

The only active component of the dislocation density tensor is

$$D_{13} = \frac{\partial \gamma}{\partial X_1}. \tag{60}$$

The equivalence of higher-order modulus A and the material parameter H_D from the $CurlF^p$ model can be derived as follows. For a crystal deforming under single-slip conditions, the plastic deformation rate is given by

$$\dot{\underset{\sim}{\boldsymbol{F}}}^p = \dot{\gamma}(\underline{\boldsymbol{m}} \otimes \underline{\boldsymbol{n}}). \tag{61}$$

Inserting (50) in (47) for $\overline{\underset{\sim}{\boldsymbol{M}}}$ gives

$$(\tau + J^p \overline{\underset{\sim}{\boldsymbol{M}}}^{(\mathrm{rel})} : \underline{\boldsymbol{m}} \otimes \underline{\boldsymbol{n}})\dot{\gamma} + X\dot{\alpha} \geq 0. \tag{62}$$

In absence of hardening variable, α, for simplicity, the generalized Schmid law for the $CurlF^p$ model, in the rate-independent case, can be defined as

$$|\tau - x| = \tau_c, \quad \text{with} \quad x = -J^p \overline{\underset{\sim}{\boldsymbol{M}}}^{(\mathrm{rel})} : \underline{\boldsymbol{m}} \otimes \underline{\boldsymbol{n}}\,. \tag{63}$$

From the specific form of the generalized stress tensor $\overline{\underset{\sim}{\boldsymbol{M}}}^{(\mathrm{rel})}$ given by (52), the back-stress x can be written as

$$x = 2H_D \mathrm{Curl}^T(\mathrm{Curl}^T(\underset{\sim}{\boldsymbol{F}}^p)) \cdot \underset{\sim}{\boldsymbol{F}}^{pT} : \underline{\boldsymbol{m}} \otimes \underline{\boldsymbol{n}}\,, \tag{64}$$

and

$$\begin{aligned}[\mathrm{Curl}^T(\mathrm{Curl}^T(\underset{\sim}{\boldsymbol{F}}^p))]_{ij} = &\begin{bmatrix} F^p_{12,12} + F^p_{13,13} & F^p_{11,21} + F^p_{13,23} & F^p_{11,31} + F^p_{12,32} \\ F^p_{22,12} + F^p_{23,13} & F^p_{21,21} + F^p_{23,23} & F^p_{21,31} + F^p_{22,32} \\ F^p_{32,12} + F^p_{33,13} & F^p_{31,21} + F^p_{33,23} & F^p_{31,31} + F^p_{32,32} \end{bmatrix} \\ - &\begin{bmatrix} F^p_{11,22} + F^p_{11,33} & F^p_{12,11} + F^p_{12,33} & F^p_{13,11} + F^p_{13,22} \\ F^p_{21,22} + F^p_{21,33} & F^p_{22,11} + F^p_{22,33} & F^p_{23,11} + F^p_{23,22} \\ F^p_{31,22} + F^p_{31,33} & F^p_{32,11} + F^p_{32,33} & F^p_{33,11} + F^p_{33,22} \end{bmatrix}. \end{aligned} \tag{65}$$

For the particular single-slip problem considered, the back-stress takes the form

$$2H_D \mathrm{Curl}^T(\mathrm{Curl}^T(\underset{\sim}{\boldsymbol{F}}^p)) \cdot \underset{\sim}{\boldsymbol{F}}^{pT} : \underline{\boldsymbol{m}} \otimes \underline{\boldsymbol{n}} = -2H_D \gamma_{,11} \tag{66}$$

Substituting (66) in (63) leads to another form of the generalized Schmid law

$$|\tau + 2H_D \gamma_{,11}\,| = \tau_c. \tag{67}$$

This equation clearly shows the emerging kinematic hardening component proportional to the second gradient of slip in the slip direction.

On the other hand, the generalized Schmid law for a single-slip problem with the Lagrange multiplier-based model can be written from (30) in the rate-independent case as

$$|\tau| + S = \tau_c. \tag{68}$$

Recalling the balance law in (12), the generalized Schmid law in (68) can be written as

$$|\tau| + \mathrm{Div}\,\underline{\boldsymbol{M}} = \tau_c. \tag{69}$$

Making use of (19) in the previous equation leads to another form of the generalized Schmid law

$$|\tau| + A(\mathrm{Div}\underline{\boldsymbol{K}}) = \tau_c, \tag{70}$$

$$A(\mathrm{Div}\underline{\boldsymbol{K}}) = A\,\mathrm{Div}\left(\frac{\partial \gamma_\chi}{\partial X_1}\underline{\boldsymbol{m}} + \frac{\partial \gamma_\chi}{\partial X_2}\underline{\boldsymbol{n}}\right) = A\frac{\partial^2 \gamma_\chi}{\partial X_2^2} = A\gamma_{,11}\,. \tag{71}$$

Finally, the form of the generalized Schmid law in (70) can be written as

$$|\tau| + A\gamma_{,11} = \tau_c. \tag{72}$$

This equation clearly shows the emerging isotropic hardening component proportional to the second gradient of slip in the slip direction. From (67) and (72), it is concluded that the higher-order moduli A and H_D can be related to each other for monotonic loading such that $\tau > 0$ and $\tau + 2H_D\gamma_{,11} > 0$. In this instance, we can identify $A = 2H_D$. The Lagrange multiplier-based model and $CurlF^p$ model are equivalent in this specific situation. It will not be the case anymore, in general, under multi-slip conditions and with consideration of the different hardening laws. Evidencing the importance of these differences is the subject of the following sections for monotonic and cyclic loading conditions.

In the presence of linear hardening with modulus H, it is possible to derive from (70) the definition of a characteristic length scale

$$\ell = \sqrt{A/|H|}, \tag{73}$$

as demonstrated in (Ling et al., 2018; Scherer et al., 2019). For more general hardening laws, a similar characteristic length scale can be defined as discussed in section 5.3.1.

5. Application to microwire torsion tests

The torsion of a single crystal microwire is characterized by two types of gradients: gradients along the radial direction from the center to outer surface and gradients along the circumferential direction as observed by Nouailhas and Cailletaud (1995). More recently, experimental investigations of microwire torsion tests on single crystal copper under monotonic loading were performed by Horstemeyer et al. (2002) with the [110] crystallographic direction being aligned with the axis of rotation. An observation of the kinematics of the deformation fields at the outer surface of the specimen was made. A wavy deformation pattern of sinusoidal waves comprising of four periods was observed and believed to be the result of four-fold symmetry of the slip plane around the circumference. Moreover, experimental assessments of polycrystalline microwire torsion tests with different specimen diameters and same grain size to study the size effects under monotonic loading were performed in (Liu et al., 2012; Guo et al., 2017). Furthermore, the experimental studies of size effects, hysteresis loops, Bauschinger effects, and anomalous plastic recovery in polycrystalline cyclic torsion tests can be found in (Liu et al., 2013; Guo et al., 2020). From a numerical point of view, size effects predictions in monotonic and cyclic loading of polycrystalline microwires were performed in (Bardella and Panteghini, 2015) using a strain gradient plasticity approach that includes the plastic spin in the constitutive framework called distortion gradient plasticity. It was observed that this theory is satisfactory to capture the size effects in monotonic loading. However, it leads to anomalous cyclic behavior in the case of cyclic loading.

In this section, the size effect predicted by the Lagrange multiplier-based model for monotonic or cyclic microwire torsion tests is compared to the predictions by the $CurlF^p$ model taken from Kaiser

and Menzel (2019a). The relation $A = 2H_D$ is used in the simulations, following the identification presented in section 4.2.

5.1. Problem setup

The simulations are performed using single crystal cylindrical microwires of height 80 mm and three different radii $R = 20$ mm, 10 mm and 5 mm, that are meshed with reduced integration 20 node brick elements (C3D20R). Note that the simulation results are not affected by the absolute values of the wire dimensions but rather by the ratio of these radii to the characteristic length scale ℓ.

The applied boundary conditions and meshed geometry are shown in Fig 2. The geometry is discretized with 3600 elements for monotonic loading and 450 elements for cyclic loading. The same finite element meshes as in (Kaiser and Menzel, 2019a) are used for the simulations performed with the Lagrange multiplier-based model in order to allow for direct comparison. The latter model was recently used to simulate torsion tests of single crystals with various orientations and finer meshes in (Scherer et al., 2020). Isotropic elasticity is considered. The bottom face of the microwire is clamped, while the top surface undergoes a rigid body rotation around the wire axis. The lateral faces are kept traction-free and free of generalized forces, which means that $\underline{\boldsymbol{T}} = 0$ and $M = 0$ in (13). The relative rotation between the upper and lower face is linearly increased to an angle of 45° for monotonic loading. For the cyclic loading test, the following conditions are enforced: The relative rotation between the upper and lower faces is first linearly increased to an angle value of 45°. Next, the relative rotation is linearly decreased to −45°. Finally, the loading is again reversed, and simulation is stopped when a relative rotation of 45° is reached. More cycles can be considered with the same relative rotation amplitudes.

The orientation of the single crystal considered is such that the [001] crystal direction is aligned with the wire axis. The basis vectors of the Cartesian coordinate system are parallel to the cubic lattice unit cell vectors:

$$\underline{\boldsymbol{e}}_1 = [100] \quad \underline{\boldsymbol{e}}_2 = [010] \quad \underline{\boldsymbol{e}}_3 = [001],$$

and are indicated in Fig. 2.

5.2. Identification of material parameters

The FCC crystal possesses the usual 12 slip systems with 6 slip directions <110> and 4 slip planes {111}.

The material parameters of the Face-Centered Cubic (FCC) single crystal for the dislocation-density based model presented in section 3.3 are now calibrated based on simple tension and simple shear predictions obtained on a single volume element with the constitutive law considered in (Kaiser and Menzel, 2019b) and recalled in section 4.1. Such a calibration is necessary because the two models compared in the present work rely on different hardening rules. The $CulF^p$ model includes a phenomenological hardening law with internal variables α whereas the reduced-order model incorporates

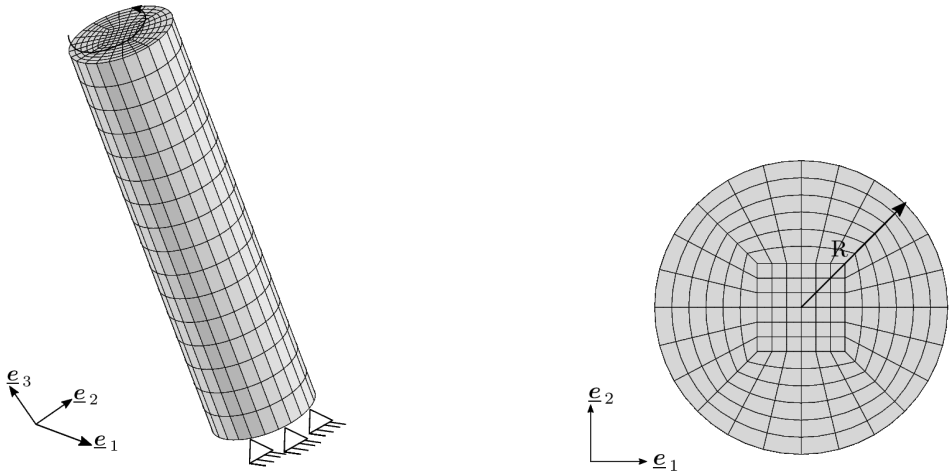

(a) (b)

Fig. 2: Microwire torsion: (a) boundary conditions (b) top view of the finite element mesh with R denoting the radius of the microwire.

Table 1: Numerical values of material parameters used for the simulation of microwire torsion tests in the reduced-order model and by Kaiser and Menzel (2019a) in the $CurlF^p$ model.

E	τ_0	m	$\dot{\gamma_0}$	μ	b
60.8 MPa	60 MPa	10	$6.0 \times 10^7\,\mathrm{s}^{-1}$	23 400 MPa	0.286 nm
G_c	κ	ϱ_0^r	h_0	h_1	h_2
100.5	10.92	5.38×10^{-11}	1.0	0	0
h_3	h_4	h_5	$a^{ru}(r \neq u)$	a^{uu}	μ_χ
0	0	0	1	0	10^3 MPa
A	τ_∞	H_0	H_D		
$10^4, 2 \times 10^4$ MPa mm^2	110 MPa	540	$5 \times 10^3, 10^4$ MPa mm^2		

evolution equations for dislocation densities. The calibrated material parameters used in the numerical simulations and the material parameters used in the $CurlF^p$ model are summarized in Table 1. The viscosity parameters are chosen in such a way that no significant rate–dependence of the results is observed in the range of strain rates considered in this work. The initial adimensional dislocation density is denoted by ϱ_0^r and assumed to be the same for all slip systems.

The corresponding tensile and shear stress-strain response of a <001> FCC single crystal is provided for both models in Fig. 3. No exact match is observed in Fig. 3 because the hardening functions are very different in both models. Only qualitative agreement is reached for the tensile and shear curves for the considered crystal orientation, which is sufficient for the comparisons performed in the sequel for torsion of bars.

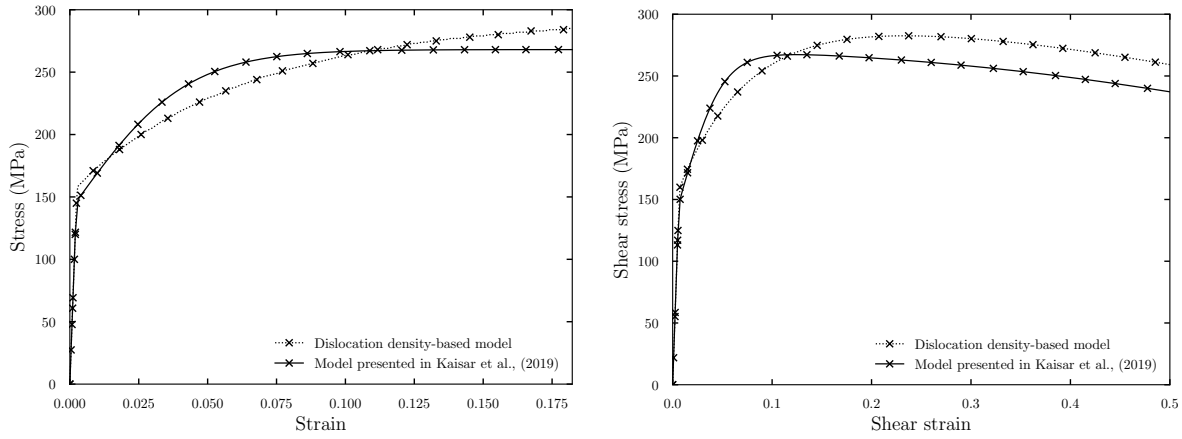

(a) (b)

Fig. 3: Constitutive response of the classical crystal plasticity formulation (section 2.2) and the material model considered in (Kaiser and Menzel, 2019b) for a <001> FCC single crystal and material parameters according to Table 1: (a) tensile test, (b) shear test. Cauchy stress components are plotted, the axial and shear strains correspond to components $F_{33}-1$ and F_{12} of the deformation gradient.

5.3. Results and discussion

The characteristic length scale ℓ considered in the simulations is defined as $\ell = \sqrt{A/|H|}$, cf. section 4.2, (73). The hardening modulus H varies during straining, and an approximate expression of the characteristic length scale is chosen to normalize the presented results. For that purpose, the initial equivalent linear hardening modulus for the tensile test is selected. Its value is given by the ratio of resolved shear stress τ^s and shear strain γ^s for one activated slip system at the beginning of its activation as proposed in Ling (2017). In the present case, the estimated H value for <001> crystal orientation is 3100 MPa. It is not possible to derive an analytical expression of the relevant characteristic length scale emerging in the torsion problem. That is why the proposed estimate is chosen.

In the following description of the results, the SSD density is defined as the sum of the 12 individual dislocations densities. The GND density is computed as the norm of the dislocation density tensor divided by b. In the $CurlF^p$ model this variable is available in the code whereas a post-processing is needed to compute the curl of plastic deformation in the case of the Lagrange multiplier-based model.

5.3.1. Comparison of predicted size effects

The comparison of the size effects predicted by the Lagrange multiplier-based model and the $CurlF^p$ model for three different values of the radius of the microwire under monotonic torsio loading using higher-order modulus $A = 20000\,\mathrm{MPa\ mm^2}$ is shown in Fig. 4a. The considered single crystal microwire is subjected to monotonic torsion loading and oriented such that the wire axis is parallel to ithe [001] crystal direction. The size-dependent curves are presented using the normalized torque

T/R^3 as a function of surface strain γ_R defined as

$$\gamma_R = kR, \tag{74}$$

where k is the applied twist per unit length θ/L. Note that this definition of γ_R is only an approximation of the actual slip value along the circumference since the plastic activity is not constant along the circumference for a cubic single crystal.

This feature can be observed in Fig. 5 which shows the cumulative plastic strain γ_{cum} fields plotted in the reference configuration. The slip activity is maximal at four locations corresponding to the direction [110] and [1$\bar{1}$0]. Fig. 4a shows that for the radii $R = 20$ mm and $R = 10$ mm, the torque vs. surface strain responses predicted by both models are almost the same, while for the radius $R = 5$ mm, the Lagrange multiplier-based model leads to a slightly harder response.

The cumulative plastic strain and dislocation density fields shown next are based on a finite element discretization with 10000 elements for a better resolution. Such fine mesh simulations could be performed only with the Lagrange multiplier-based model. The computational efficiency of the Lagrange multiplier-based model in terms of CPU time allows faster computation of size effect even with finer mesh discretization. Fig. 6 and 7 respectively show the spatial distributions of the SSD and GND density for the three considered radii. It is observed that the dislocation density multiplication starts at the free surface of the microwire and is driven towards the center. During the deformation process, the evolution of the SSD density is due to the dislocation generation and annihilation mechanism. The initial dislocation density $\rho^r (= \varrho^u/b^2)$ is assumed to be $6.5 \times 10^8\,\mathrm{m}^{-2}$ and chosen the same for all slip systems. Distinct four-fold patterns of the SSD density distribution are observed for all three radii of the microwire. On the other hand, the GND density distribution shows distinct four-fold patterns for the radii $R = 5\,\mathrm{mm}$ and $R = 10\,\mathrm{mm}$, while it shows more localized distribution for $R = 20\,\mathrm{mm}$ making the four-fold symmetry of FCC single-crystal almost disappear.

The SSD and GND density distributions at different stages of the relative rotation are shown in Fig. 8 and 9, respectively. At the initial stage of the deformation, the maximum SSD density is observed at four locations corresponding to the [110] crystal direction (see Fig. 8a). However, as the deformation progresses, the maximal dislocation density locations are observed at the corresponding [100] crystal direction as shown in Fig. 8c for the relative rotation of 22.5°. With the deformation, the difference between the magnitude of the maximal and minimal increment of the cumulative plastic strain, $\sum_{r=1}^{N} |\triangle\gamma^r|$, along the circumference decreases and the field becomes almost homogeneous. This may explain the shift in the maximal SSD density locations with the deformation. On the other hand, at the initial stage of the relative rotation, the GND density is maximal at four locations around the directions [100] (see Fig. 9a) and remains at the corresponding [100] crystal direction with further increase in the relative rotation (see Fig. 9c). Moreover, it is observed that there is a slight evolution of the GND density field with more localized distribution compared to the SSD density field.

Fig. 10a and 10b show the profiles of the cumulative plastic strain γ_{cum} for three different radii along the circumferential and radial directions, respectively. For the given relative rotation angle,

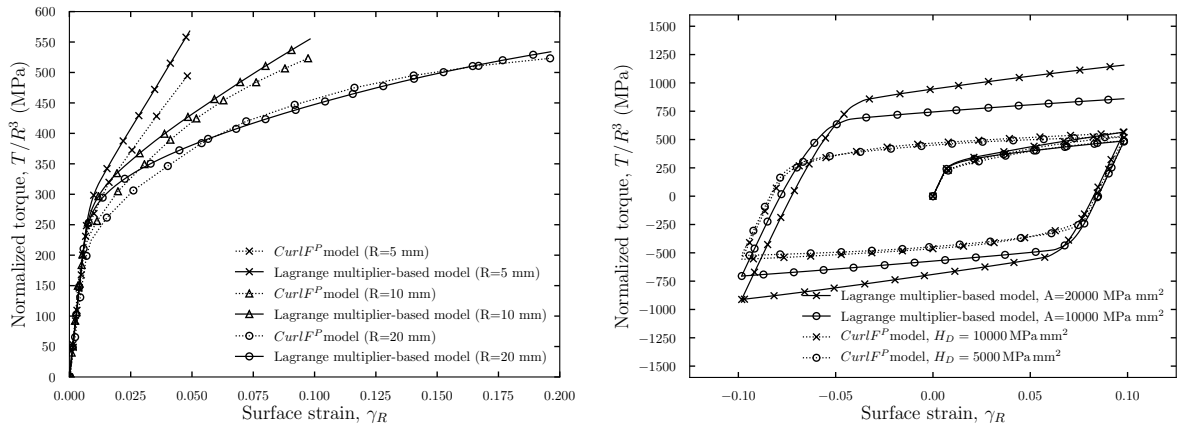

(a) (b)

Fig. 4: Comparison of normalized torque vs. surface strain curves (<001> crystal orientation, $R = 10$ mm), for the Lagrange multiplier-based model and the $CurlF^p$ model: (a) monotonic loading, and (b) cyclic loading.

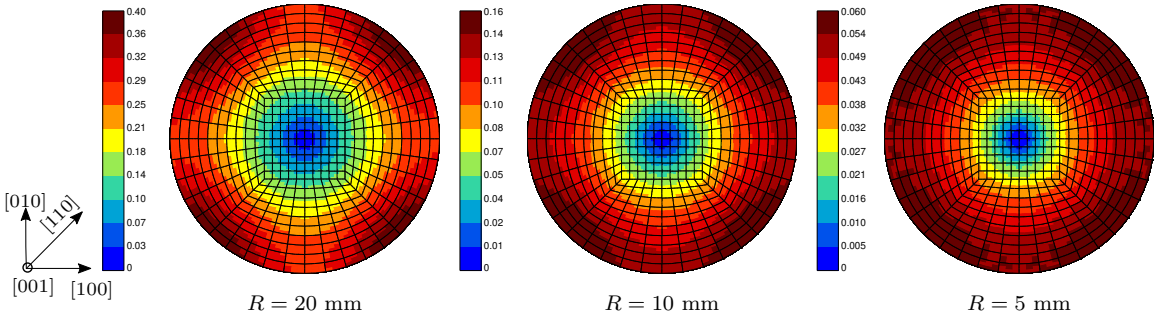

Fig. 5: Cumulative plastic strain field in <001> FCC single crystal predicted by the Lagrange multiplier-based model with $A = 20000\,\text{MPa mm}$ and a finite element discretization featuring 10000 elements. The results for an applied relative rotation of 45° between the upper and lower faces are shown on the undeformed configuration.

distinct four-fold patterns of the plastic strain field can be observed for $R = 20\,\text{mm}$ and $R = 10\,\text{mm}$. The plastic strain field is smoother along the circumference for $R = 5\,\text{mm}$ because the smaller radius gives a stiffer response and limits the strain localization in these zones. The radial distributions in Fig. 10b are almost linear.

The comparison of the size effect predicted by the Lagrange multiplier-based model and the $CurlF^p$ model in the case of cyclic loading conditions is shown in Fig. 4b. These simulations were performed for two values of the higher-order modulus, namely $A = 10000\,\text{MPa mm}^2$ and $20000\,\text{MPa mm}^2$. The ratio $A = 2H_D$ is kept constant in both cases to allow for the comparison of both models. The Lagrange multiplier-based model predicts isotropic hardening as shown in Fig. 4b. In contrast, the higher-order stresses act as a back-stress in the $CurlF^p$ model, resulting in kinematic hardening. Fig. 11a shows the saturation of cyclic curves after 5 cycles using classical crystal plasticity model with dislocation density-based hardening. In contrast, the gradient effect associated with parameter A

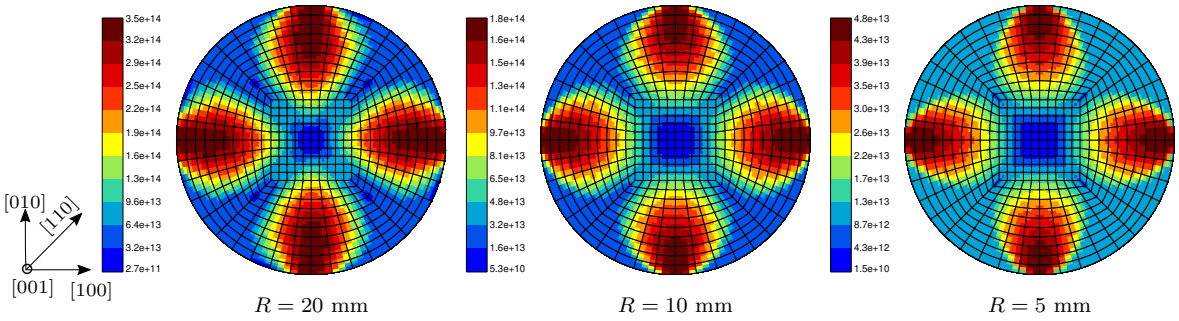

Fig. 6: SSD density distribution in FCC single crystal (<100> crystal orientation) predicted by the Lagrange multiplier-based model with $A = 20000\,\text{MPa mm}^2$ and a finite element discretization featuring 10000 elements. The results for an applied relative rotation of 45° between the upper and lower faces are shown on the undeformed configuration.

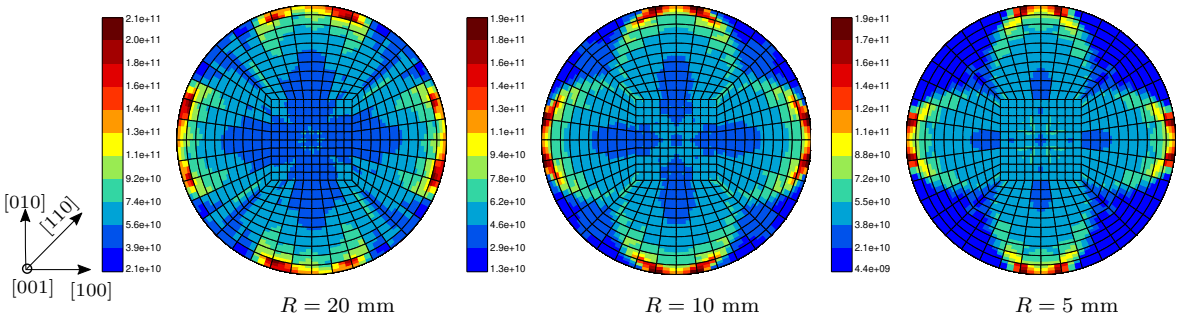

Fig. 7: GND density distribution in FCC single crystal (<100> crystal orientation) predicted by the Lagrange multiplier-based model with $A = 20000\,\text{MPa mm}^2$ and a finite element discretization featuring 10000 elements. The results are shown on the undeformed configuration for an applied relative rotation of 45° between the upper and lower faces.

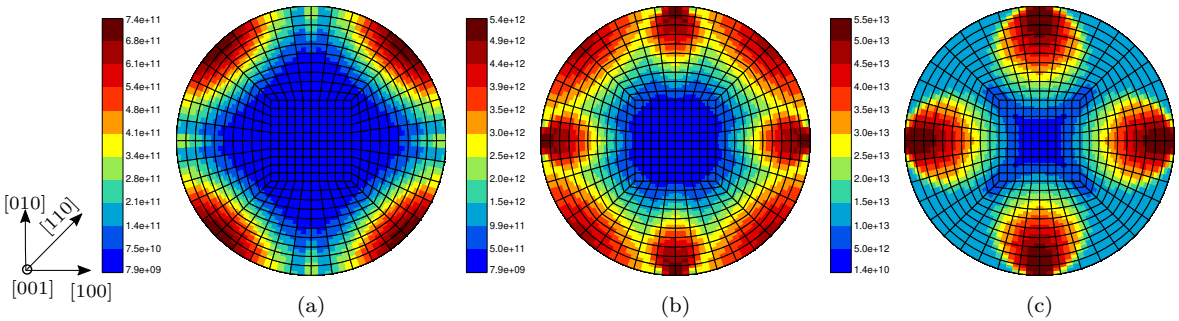

Fig. 8: SSD density distribution in FCC single crystal (<100> crystal orientation, $R = 10$ mm) predicted by the Lagrange multiplier-based model with $A = 20000\,\text{MPa mm}^2$ and a finite element discretization featuring 10000 elements at an applied relative rotation of (a) 4.5° (b) 9° and (c) 22.5° shown on the undeformed configuration.

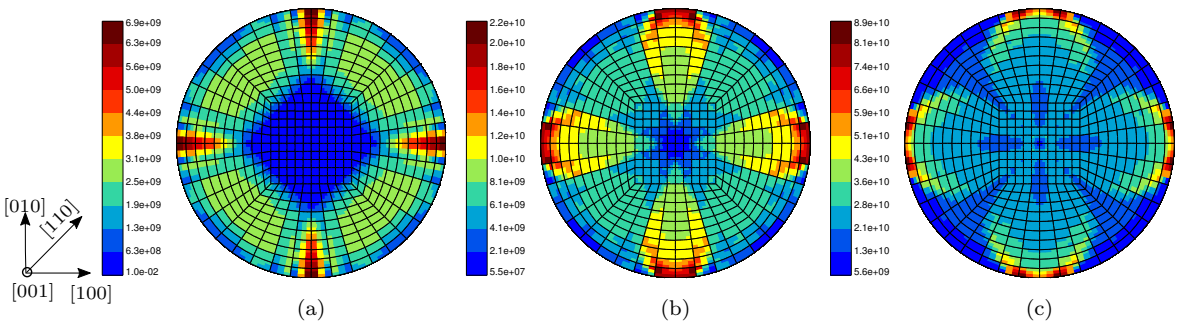

(a) (b) (c)

Fig. 9: GND density distribution in FCC single crystal (<100> crystal orientation, $R = 10$ mm) predicted by the Lagrange multiplier-based model with $A = 20000\,\text{MPa mm}^2$ at an applied relative rotation of (a) 4.5° (b) 9° and (c) 22.5° shown on the undeformed configuration.

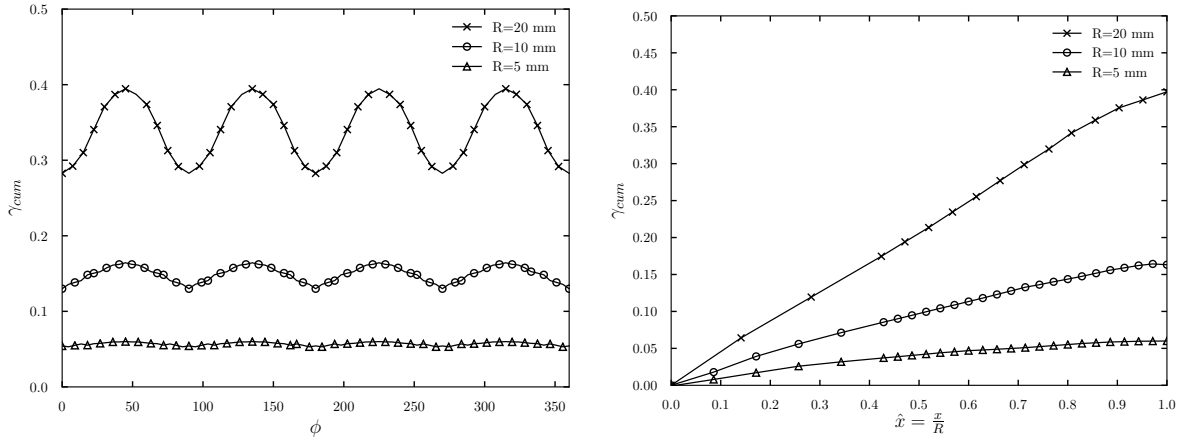

(a) (b)

Fig. 10: Cumulative plastic strain γ_{cum} profiles predicted by a Lagrange multiplier-based model along the (a) circumferential and (b) radial direction of the microwire for monotonic loading and for three radii of microwire using A=20000 MPa mm^2. The radial distance from the center of the specimen is denoted by x and the radius of the microwire by R.

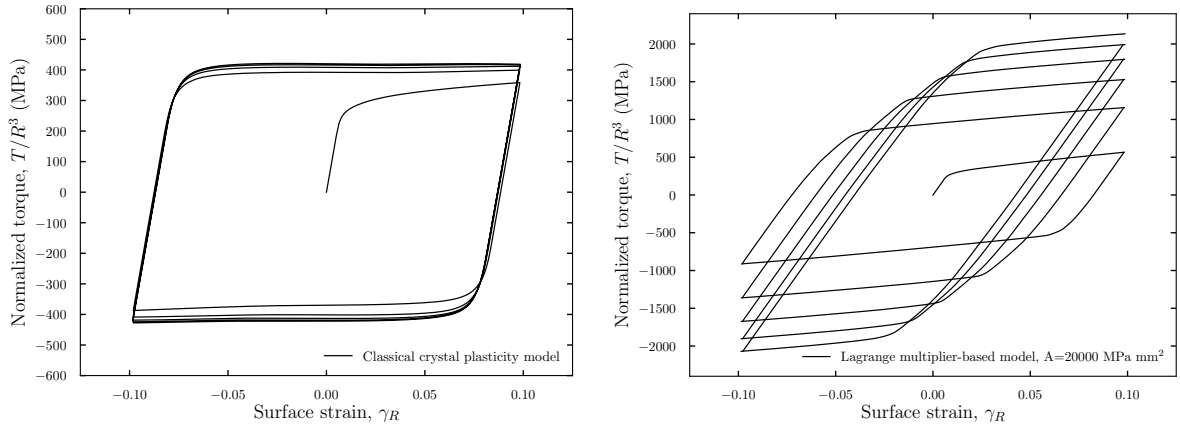

Fig. 11: Comparison of normalized torque vs. surface strain curves for <001> crystal orientation and for cyclic loading using (a) a classical crystal plasticity formulation according to section 2.2, and (b) Lagrange multiplier-based model using $A = 20000\,\mathrm{MPa\,mm^2}$. The microwire of radius $R = 10$ mm discretized using 3600 finite elements.

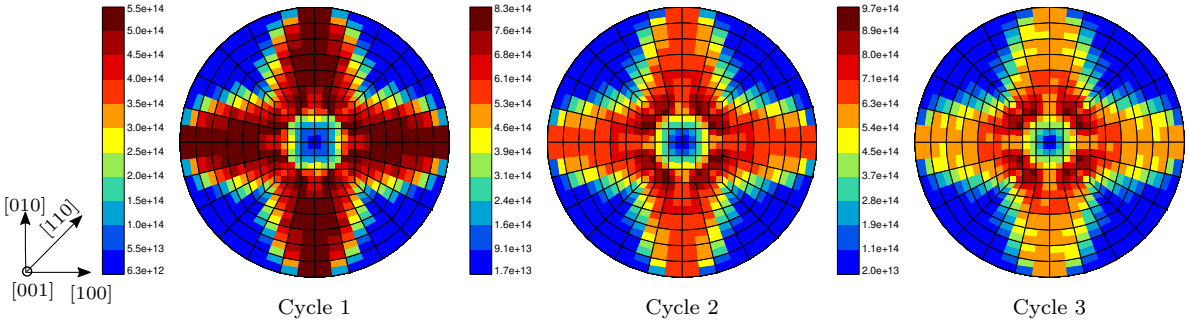

Fig. 12: SSD density distribution in FCC single crystal bar under cyclic torsion (<100> crystal orientation, $R = 10$ mm, $A = 20000\,\mathrm{MPa\,mm^2}$) predicted by the Lagrange multiplier-based model and a finite element discretization featuring 3600 elements.

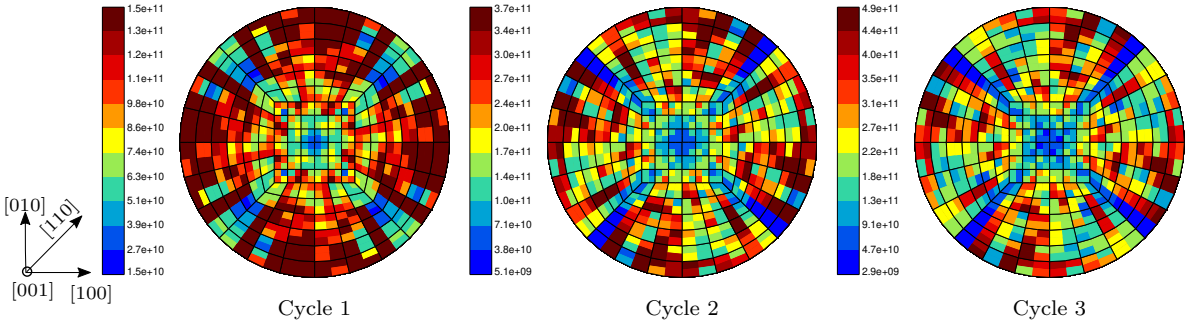

Fig. 13: GND density distribution in FCC single crystal (<100> crystal orientation, $R = 10$ mm, $A = 20000\,\mathrm{MPa\,mm^2}$) predicted by the Lagrange multiplier-based model and a finite element discretization featuring 3600 elements.

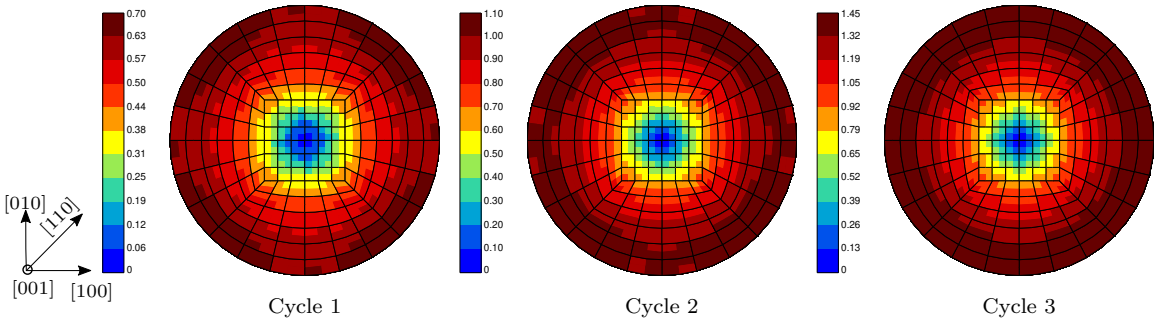

Fig. 14: Cumulative plastic strain γ_{cum} distribution in FCC single crystal bar under cyclic torsion (<100> crystal orientation, $R = 10$ mm) predicted by the Lagrange multiplier-based model with $A = 20000\,\mathrm{MPamm}^2$ and a finite element discretization featuring 3600 elements.

leads to strong additional isotropic hardening as depicted in Fig. 11b with no apparent saturation.

The cumulative plastic strain and dislocation density fields shown next are plotted for the microwire of radius $R = 10\,\mathrm{mm}$ and based on a finite element discretization with 3600 elements. Fig. 12 and 13 show the SSD and GND density distribution over the cross section at the end of each cycle. As the deformation progresses, the dislocation density significantly increases with the plastic strain, and SSD density gets much larger than GND density. In particular, the SSD and GND densities increase from an initial value of $6.5 \times 10^8\,\mathrm{m}^{-2}$ to $9.7 \times 10^{14}\,\mathrm{m}^{-2}$ and from 0 to $4.9 \times 10^{11}\,\mathrm{m}^{-2}$, respectively at the end of cycle 3. In addition, the dislocation density distribution maintains the distinct four-fold symmetry pattern even at the end of cycle 3. After cycling, the GND density field does not display clear patterns any more, see Fig. 13. A finer mesh would be necessary for a better resolutin of the gradients.

The plastic strain distribution and profiles along the circumferential and radial directions for cyclic loading are shown in Fig. 14 and 15. Accumulation of plastic deformation during cycling in the four zones of favored plastic slip leads to increased gradient values and subsequent additional hardening, thus explaining the cyclic hardening of Fig. 11b. With further increase in number of cycles, the cumulative plastic strain increases and becomes almost homogeneous along the circumference, making the four-fold symmetry of FCC single crystal almost disappear as shown in Fig. 14 and 15a. This may explain the trend to some saturation of cyclic hardening in Fig. 11b. It is observed that the magnitude of the plastic strain field increases in the radial direction with an increasing number of cycles as shown in Fig. 15b.

5.3.2. Scaling law

In this section, the scaling behavior is studied for the micromorphic model presented in section 3.1 and the Lagrange multiplier-based model presented in section 3.2. The dependence of the normalized torque on the R/ℓ is analyzed for the monotonic microwire torsion tests. The simulations are performed for several radii of the microwire ranging from $R = 2$ mm to $R = 30$ mm and using the value

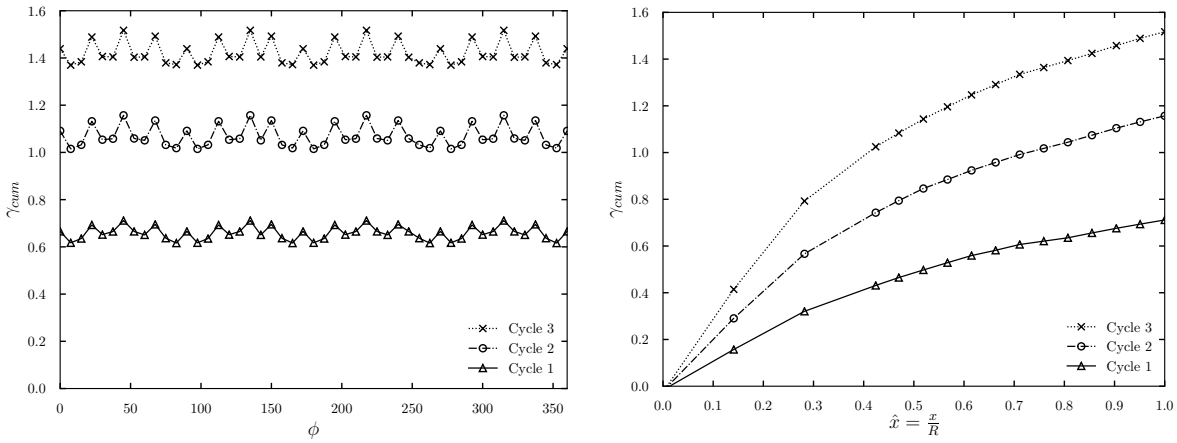

(a) (b)

Fig. 15: Cumulative plastic strain γ_{cum} variation along the (a) circumferential and (b) radial direction of the microwire for cyclic loading using Lagrange multiplier-based model (A=20000 MPa mm^2, R = 10 mm, and a finite element discretization with 3600 elements). The radial distance from the center of the specimen is denoted by x and the radius of the microwire by R.

of the higher-order modulus $A = 20000\,\text{MPa}\,\text{mm}^2$. The scaling laws in the form of the power law $T/R^3 \propto (R/\ell)^n$ for microwire torsion tests characterizing the effect of the R/ℓ ratio on the normalized torque T/R^3 are shown in Fig 16a. The characteristic length scale ℓ defined as $\sqrt{A/|H|}$ is 2.55 mm. The log-log plot of the normalized torque values as a function of R/ℓ ratio at a surface strain of 0.01 are plotted in Fig. 16b for the reduced-order micromorphic model using $H_\chi = 10^4$ MPa and $H_\chi = 3 \times 10^4$ MPa, and for the Lagrange multiplier-based model using $\mu_\chi = 10^3$ MPa, respectively. For lower values of the coupling modulus H_χ the micromorphic model predicts a typical *tanh* shape (Cordero et al., 2010) with saturation for small ($R/\ell < 0.8$) and large ($R/\ell > 0.8$) values of the R/ℓ ratio. The slope of the bounded intermediate regime for the micromorphic model using $H_\chi = 10^4\,\text{MPa}$ and $H_\chi = 3\times10^4\,\text{MPa}$ is found to be $n = -0.6$ and $n = -0.85$, respectively. The Lagrange multiplier-based model can be considered as a limiting case of a micromorphic model for large values of H_χ, which leads to a power-law exponent $n = -1.0$ of asymptotic regime towards zero. In the latter case, no saturation is expected.

The power-law exponent n of the micromorphic model depends on the material parameters H_χ and A, whereas it is independent of material parameters in the Lagrange multiplier-based model. The critical value of the R/ℓ ratio is defined by the inflection point i of the plot in Fig 16b. The value of i depends on the coupling modulus H_χ and is found to be 4 and 3 for $H_\chi = 10^4\,\text{MPa}$ and $H_\chi = 3 \times 10^4\,\text{MPa}$, respectively, which represents the size-dependent domain of material response.

6. Conclusion

The objective of the present was to compare the response in torsion at finite deformations of three size-dependent models recently published in the literature: a gradient crystal plasticity model involving

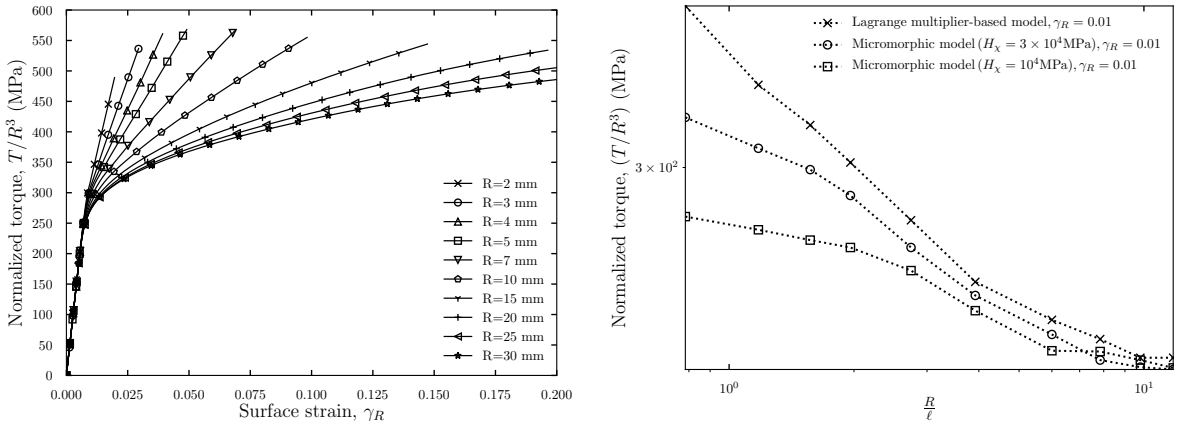

(a) (b)

Fig. 16: Normalized torque vs. surface strain curves for <001> crystal orientation: (a) influence of the microwire radius when using a Lagrange multiplier-based model,(b) normalized torque as a function of R/ℓ at a surface strain γ_R of 0.01 for micromorphic and Lagrange multiplier-based models.

the complete dislocation density tensor by Kaiser and Menzel (2019a), a reduced-order micromorphic crystal plasticity model and a Lagrange multiplier-based gradient crystal plasticity model described in (Scherer et al., 2020). Results previously obtained by Kaiser and Menzel (2019a) were compared to new simulations carried out with the two other models. A detailed analysis of the evolution of plastic strain, SSD and GND density fields was provided. The main findings obtained in this contribution can be summarized as follows:

1. The size effects predicted by the Lagrange multiplier-based model were found to be in good agreement with the predictions made by the $CurlF^p$ model in the case of monotonic torsion of a cylindrical bar with axis parallel to [001] crystal direction.
2. Gradient effects tend to reduce the strain heterogeneity which arises in torsion along the circumference. This effect is predicted by all three models.
3. Interesting evolutions of the SSD vs GND densities during monotonic torsion were evidenced. The location of maximal SSD density values was shown to change from $< 011 >$ to $< 100 >$ positions along the circumference when increasing the twist angle. In contrast the maximal GND density values remain around $< 100 >$ positions.
4. The Lagrange multiplier-based model induces isotropic hardening in cyclic torsion because it is based on the gradient of a scalar-valued cumulative plastic strain variable. This is in contrast to the kinematic hardening induced by the $CurlF^p$ model due to the back-stress resulting from the action of higher-order stresses. This leads to significantly different responses under cyclic loading conditions.
5. The analysis of the cyclic torsion tests shows the evolution of plastic slip gradients along the circumference with a trend towards more homogeneous distributions for larger cycle numbers according to the Lagrange multiplier-based model. A significant increase in SSD and GND

densities is observed at the end of each cycle compared to previous cycles.

6. The size effects are characterized by power law relationships between the normalized torque and R/ℓ, with ℓ being a characteristic length of the model. The reduced micromorphic model saturates for small and large values of this ratio. It possesses an intermediate domain with powers $n = -0.6$ and $= -0.85$, which were found for $H_\chi = 10^4$ MPa and $H_\chi = 3 \times 10^4$ MPa, respectively. In contrast, the augmented Lagrangian version of the model, which corresponds to a strict strain gradient plasticity model, predicts no saturation at small R/ℓ ratios and a power law with $n = -1$.

An equivalence between the reduced-order Lagrange multiplier-based model and the $CurlF^p$ model exists in the case of a single-slip under monotonic loading. The $CurlF^p$ model has a clear physical interpretation in terms of the dislocation density tensor in contrast to the reduced-order models, which incorporate the gradient of cumulative slip in a purely phenomenological way. Reduced-order models are advantageous from a computational point of view and lead to significantly lower computation times in the presented examples. The computational efficiency in terms of CPU time of the Lagrange multiplier-based model and of the micromorphic model that was studied in this contribution is investigated in (Scherer et al., 2020). The $CurlF^p$ model, which includes 21 DOFs at each node in three-dimensional settings, is computationally expensive compared to the Lagrange multiplier-based model, which requires 5 DOFs per node. It has been demonstrated that the $CurlF^p$ and reduced-order models can deliver similar predictions in terms of hardening and size effects, at least for monotonic tests. The reduced-order models can therefore be applied for faster evaluation of size effects in structural computations. More physical understanding can be gained using the full gradient model.

The full gradient and reduced-order models could further be compared in the case of localization phenomena in crystalline materials as recently explored by Marano et al. (2021). Regularization of strain localization phenomena in single crystals such as slip, kink and shear bands was demonstrated in (Ling et al., 2018).

A limitation of the reduced-order micromorphic and Lagrange multiplier-based formulations presented in this work is that the gradient terms essentially affect the isotropic hardening and do not incorporate a size-dependent back-stress, in contrast to full-order micromorphic and the gradient plasticity models. The simulation of kinematic-type hardening is, in fact, possible with a reduced-order model using an alternative formulation in which the free energy potential depends on the gradient of the microslip variable as pointed out in (Forest, 2016; Ling et al., 2018). Another possibility is to consider the gradient of the equivalent plastic strain instead of the cumulative one. This will cause size-dependent kinematic hardening effects, as recently demonstrated by Jebahi and Forest (2021).

Appendix A Summary of constitutive equations in reduced-order and $CurlF^p$ models

The constitutive equations used in the reduced-order and the $CurlF^p$ models are summarized in Table 2.

Table 2: Summary of constitutive equations used in reduced-order and the $CurlF^p$ models.

Constitutive equations	Reduced-order model (Lagrange multiplier-based)	$CurlF^p$ model
DOF (three-dimensional setting)	$\{\underline{\boldsymbol{u}}, \gamma_\chi, \lambda\}$ Total DOF per node = 5	$\{\underline{\boldsymbol{u}}, \overline{\underset{\sim}{\boldsymbol{M}}}^{(\mathrm{rel})}, \underset{\sim}{\boldsymbol{\theta}}^p\}$ Total DOF per node = 21
Free energy density function	$L_0(\underset{\sim}{\boldsymbol{E}}^e_{GL}, e, \underline{\boldsymbol{K}}, \lambda, \alpha)$	$\Psi = \tilde{\Psi}(\underset{\sim}{\boldsymbol{F}}, \underset{\sim}{\boldsymbol{F}}^p, \underset{\sim}{\boldsymbol{D}}, \alpha)$
State laws	$\underset{\sim}{\boldsymbol{\Pi}}^e = \rho_\# \frac{\partial L_0}{\partial \underset{\sim}{\boldsymbol{E}}^e_{GL}}$ $S = -\rho_0 \frac{\partial L_0}{\partial e}$ $\underline{\boldsymbol{M}} = \rho_0 \frac{\partial L_0}{\partial \underline{\boldsymbol{K}}}$ $X = -\rho_0 \frac{\partial L_0}{\partial \alpha}$	$\underset{\sim}{\boldsymbol{P}} = \rho_\# \frac{\partial \tilde{\Psi}}{\partial \underset{\sim}{\boldsymbol{F}}}$ $\underset{\sim}{\boldsymbol{\Xi}} = -\rho_0 \frac{\partial \tilde{\Psi}}{\partial \underset{\sim}{\boldsymbol{D}}}$ $X = -\rho_0 \frac{\partial \Psi}{\partial \alpha}$
Balance laws	$\mathrm{Div}\, \underset{\sim}{\boldsymbol{S}} = 0$ and $\mathrm{Div}\, \underline{\boldsymbol{M}} - S = 0$, $\forall\, \underline{\boldsymbol{X}} \subset \Omega^0$	$J^p \overline{\underset{\sim}{\boldsymbol{M}}} = J^p \underset{\sim}{\boldsymbol{\Pi}}^M + \mathrm{Curl}(\underset{\sim}{\boldsymbol{\Xi}}) \cdot \underset{\sim}{\boldsymbol{F}}^{pT} = 0$, in B^0_{dis}
Boundary conditions	$\underline{\boldsymbol{T}} = \underset{\sim}{\boldsymbol{S}} \cdot \underline{\boldsymbol{N}}$ and $M = \underline{\boldsymbol{M}} \cdot \underline{\boldsymbol{N}}$, $\forall\, \underline{\boldsymbol{X}} \subset \partial\Omega^0$	$\underset{\sim}{\boldsymbol{\Xi}} \cdot \mathrm{Spn}(\underline{\boldsymbol{N}}) \cdot \underset{\sim}{\boldsymbol{F}}^{pT} = 0$, on $\partial B^0_{dis,ext}$
Residual dissipation inequality	$J^p \underset{\sim}{\boldsymbol{\Pi}}^M : (\dot{\underset{\sim}{\boldsymbol{F}}}^p \cdot \underset{\sim}{\boldsymbol{F}}^{p-1}) + S\dot{\gamma}_{cum}$ $+X\dot{\alpha} \geq 0$	$J^p \underset{\sim}{\boldsymbol{\Pi}}^M : (\dot{\underset{\sim}{\boldsymbol{F}}}^p \cdot \underset{\sim}{\boldsymbol{F}}^{p-1}) + \underset{\sim}{\boldsymbol{\Xi}} : \dot{\underset{\sim}{\boldsymbol{D}}}$ $+X\dot{\alpha} \geq 0$
Thermodynamic force associate with the internal hardening variable	$X = -\mu\xi\sqrt{\sum_{u=1}^N h^{ru} \varrho^u}$	$X = -\left(\tau_0 + (\tau_\infty - \tau_0)\tanh\left(\frac{h_0 \alpha}{\tau_\infty - \tau_0}\right)\right)$
Material parameters related to characteristic length scale	A	H_D

Acknowledgements

The research leading to these results has received funding from the European Union's Horizon 2020 research and innovation program, Marie Sklodowska-Curie Actions, under grant agreement no. 764979, project "ENABLE," "European Network for Alloys Behaviour Law Enhancement."

References

Abrivard, G., Busso, E., Forest, S., Appolaire, B., 2012. Phase field modelling of grain boundary motion driven by curvature and stored energy gradients. part i: theory and numerical implementation. Philosophical Magazine 92, 3618–3642.

Acharya, A., Bassani, J., 2000. Lattice incompatibility and a gradient theory of crystal plasticity. Journal of the Mechanics and Physics of Solids 48, 1565–1595. doi:https://doi.org/10.1016/S0022-5096(99)00075-7.

Anand, L., Aslan, O., Chester, S.A., 2012. A large-deformation gradient theory for elastic–plastic materials: Strain softening and regularization of shear bands. International Journal of Plasticity 30-31, 116–143. doi:https://doi.org/10.1016/j.ijplas.2011.10.002.

Anand, L., Kothari, M., 1996. A computational procedure for rate-independent crystal plasticity. Journal of the Mechanics and Physics of Solids 44, 525–558. doi:https://doi.org/10.1016/0022-5096(96)00001-4.

Ashby, M.F., 1970. The deformation of plastically non-homogeneous materials. The Philosophical Magazine: A Journal of Theoretical Experimental and Applied Physics 21, 399–424. doi:https://doi.org/10.1080/14786437008238426.

Aslan, O., Cordero, N.M., Gaubert, A., Forest, S., 2011. Micromorphic approach to single crystal plasticity and damage. International Journal of Engineering Science 49, 1311–1325. doi:https://doi.org/10.1016/j.ijengsci.2011.03.008.

Bardella, L., Panteghini, A., 2015. Modelling the torsion of thin metal wires by distortion gradient plasticity. Journal of the Mechanics and Physics of Solids 78, 467–492. doi:https://doi.org/10.1016/j.jmps.2015.03.003.

Bayley, C., Brekelmans, W., Geers, M., 2006. A comparison of dislocation induced back stress formulations in strain gradient crystal plasticity. International Journal of Solids and Structures 43, 7268–7286. doi:10.1016/j.ijsolstr.2006.05.011.

Bilby, B.A., Bullough, R., Smith, E., Whittaker, J.M., 1955. Continuous distributions of dislocations: a new application of the methods of non-riemannian geometry. Proceedings of the Royal Society of London. Series A. Mathematical and Physical Sciences 231, 263–273. doi:https://doi.org/10.1098/rspa.1955.0171.

Bittencourt, E., Needleman, A., Gurtin, M., Van der Giessen, E., 2003. A comparison of nonlocal continuum and discrete dislocation plasticity predictions. Journal of the Mechanics and Physics of Solids 51, 281–310. doi:https://doi.org/10.1016/S0022-5096(02)00081-9.

Brepols, T., Wulfinghoff, S., Reese, S., 2017. Gradient-extended two-surface damage-plasticity: Micromorphic formulation and numerical aspects. International Journal of Plasticity 97, 64–106. doi:https://doi.org/10.1016/j.ijplas.2017.05.010.

Busso, E., Meissonnier, F., O'Dowd, N., 2000. Gradient-dependent deformation of two-phase single crystals. Journal of the Mechanics and Physics of Solids 48, 2333–2361. doi:https://doi.org/10.1016/S0022-5096(00)00006-5.

Busso, E.P., Cailletaud, G., 2005. On the selection of active slip systems in crystal plasticity. International Journal of Plasticity 21, 2212–2231. doi:https://doi.org/10.1016/j.ijplas.2005.03.019.

Cermelli, P., Gurtin, M.E., 2001. On the characterization of geometrically necessary dislocations in finite plasticity. Journal of the Mechanics and Physics of Solids 49, 1539–1568.

Cordero, N., Forest, S., Busso, E., Berbenni, S., Cherkaoui, M., 2012. Grain size effects on plastic strain and dislocation density tensor fields in metal polycrystals. Computational Materials Science 52, 7–13. doi:https://doi.org/10.1016/j.commatsci.2011.02.043.

Cordero, N.M., Gaubert, A., Forest, S., Busso, E.P., Gallerneau, F., Kruch, S., 2010. Size effects in generalised continuum crystal plasticity for two-phase laminates. Journal of the Mechanics and Physics of Solids 58, 1963–1994. doi:https://doi.org/10.1016/j.jmps.2010.06.012.

Dillard, T., Forest, S., Ienny, P., 2006. Micromorphic continuum modelling of the deformation and fracture behaviour of nickel foams. European Journal of Mechanics A/Solids 25, 526–549. doi:https://doi.org/10.1016/j.euromechsol.2005.11.006.

Erdle, H., Böhlke, T., 2017. A gradient crystal plasticity theory for large deformations with a discontinuous accumulated plastic slip. Computational Mechanics 60, 923–942. doi:10.1007/s00466-017-1447-7.

Eringen, A.C., 1999. Microcontinuum field theories. Springer, New York.

Fleck, N., Hutchinson, J., 1993. A phenomenological theory for strain gradient effects in plasticity. Journal of the Mechanics and Physics of Solids 41, 1825–1857. doi:https://doi.org/10.1016/0022-5096(93)90072-N.

Fleck, N., Muller, G., Ashby, M., Hutchinson, J., 1994. Strain gradient plasticity: Theory and experiment. Acta Metallurgica et Materialia 42, 475–487. doi:https://doi.org/10.1016/0956-7151(94)90502-9.

Forest, S., 2009. Micromorphic approach for gradient elasticity, viscoplasticity, and damage. Journal of Engineering Mechanics 135, 117–131. doi:10.1061/(asce)0733-9399(2009)135:3(117).

Forest, S., 2016. Nonlinear regularization operators as derived from the micromorphic approach to gradient elasticity, viscoplasticity and damage. Proc. R. Soc. A 472, 20150755. doi:https://doi.org/10.1098/rspa.2015.0755.

Fortin, M., Glowinski, R., 1983. Chapter iii on decomposition-coordination methods using an augmented lagrangian, in: Studies in Mathematics and Its Applications. Elsevier. volume 15, pp. 97–146. doi:https://doi.org/10.1016/S0168-2024(08)70028-6.

Gao, H., Huang, Y., Nix, W., Hutchinson, J., 1999. Mechanism-based strain gradient plasticity— i. theory. Journal of the Mechanics and Physics of Solids 47, 1239–1263. doi:https://doi.org/10.1016/S0022-5096(98)00103-3.

Geers, M., Peerlings, R., Brekelmans, W., 2000. Phenomenological nonlocal approaches based on implicit gradient-enhanced damage. Acta Mechanica 144, 1–15. doi:https://doi.org/10.1007/BF01181824.

Guo, S., He, Y., Lei, J., Li, Z., Liu, D., 2017. Individual strain gradient effect on torsional strength of electropolished microscale copper wires. Scripta Materialia 130, 124–127. doi:https://doi.org/10.1016/j.scriptamat.2016.11.029.

Guo, S., He, Y., Tian, M., Liu, D., Li, Z., Lei, J., Han, S., 2020. Size effect in cyclic torsion of micron-scale polycrystalline copper wires. Materials Science and Engineering: A 792, 139671. doi:https://doi.org/10.1016/j.msea.2020.139671.

Gurtin, M.E., 2002. A gradient theory of single-crystal viscoplasticity that accounts for geometrically necessary dislocations. Journal of the Mechanics and Physics of Solids 50, 5–32. doi:https://doi.org/10.1016/S0022-5096(01)00104-1.

Horstemeyer, M., Lim, J., Lu, W.Y., Mosher, D., Baskes, M., Prantil, V., Plimpton, S., 2002. Torsion/simple shear of single crystal copper. Journal of Engineering Materials and Technology-transactions of The Asme 124. doi:10.1115/1.1480407.

Jebahi, M., Forest, S., 2021. Scalar-based strain gradient plasticity theory to model size-dependent kinematic hardening effects. Continuum Mechanics and Thermodynamics doi:10.1007/s00161-020-00967-0.

Kaiser, T., Menzel, A., 2019a. A dislocation density tensor-based crystal plasticity framework. Journal of the Mechanics and Physics of Solids 131, 276–302. doi:https://doi.org/10.1016/j.jmps.2019.05.019.

Kaiser, T., Menzel, A., 2019b. An incompatibility tensor-based gradient plasticity formulation-Theory and numerics. Computer Methods in Applied Mechanics and Engineering 345, 671–700. doi:https://doi.org/10.1016/j.cma.2018.11.013.

Kubin, L., Devincre, B., Hoc, T., 2008. Modeling dislocation storage rates and mean free paths in face-centered cubic crystals. Acta Materialia 56, 6040–6049. doi:https://doi.org/10.1016/j.actamat.2008.08.012.

Lee, E.H., Liu, D.T., 1967. Finite strain elastic plastic theory with application to plane wave analysis. Journal of Applied Physics 38, 19–27. doi:https://doi.org/10.1063/1.1708953.

Liebe, T., Menzel, A., Steinmann, P., 2003. Theory and numerics of geometrically non-linear gradient plasticity. International Journal of Engineering Science 41, 1603–1629. doi:https://doi.org/10.1016/S0020-7225(03)00030-2. damage and failure analysis of materials.

Ling, C., 2017. Modeling the intragranular ductile fracture of irradiated steels. Effects of crystal anisotropy and strain gradient. Theses. PSL Research University. URL: https://pastel.archives-ouvertes.fr/tel-01699226.

Ling, C., Forest, S., Besson, J., Tanguy, B., Latourte, F., 2018. A reduced micromorphic single crystal plasticity model at finite deformations. application to strain localization and void growth in ductile metals. International Journal of Solids and Structures 134, 43–69. doi:https://doi.org/10.1016/j.ijsolstr.2017.10.013.

Liu, D., He, Y., Dunstan, D.J., Zhang, B., Gan, Z., Hu, P., Ding, H., 2013. Anomalous plasticity in the cyclic torsion of micron scale metallic wires. Phys. Rev. Lett. 110, 244301. doi:10.1103/PhysRevLett.110.244301.

Liu, D., He, Y., Tang, X., Ding, H., Hu, P., Cao, P., 2012. Size effects in the torsion of microscale copper wires: Experiment and analysis. Scripta Materialia 66, 406–409. doi:https://doi.org/10.1016/j.scriptamat.2011.12.003.

Mandel, J., 1973. Equations constitutives et directeurs dans les milieux plastiques et viscoplastiques. Int. J. Solids Structures 9, 725–740. doi:https://doi.org/10.1016/0020-7683(73)90120-0.

Marano, A., Gélébart, L., Forest, S., 2021. FFT-based simulations of slip and kink bands formation in 3D polycrystals: influence of strain gradient crystal plasticity. Journal of the Mechanics and Physics of Solids 149, 104295. doi:https://doi.org/10.1016/j.jmps.2021.104295.

Mayeur, J., McDowell, D., 2014. A comparison of gurtin type and micropolar theories of generalized single crystal plasticity. International Journal of Plasticity 57, 29–51. doi:https://doi.org/10.1016/j.ijplas.2014.01.010.

Mayeur, J.R., McDowell, D.L., Bammann, D.J., 2011. Dislocation-based micropolar single crystal plasticity: Comparison of multi- and single criterion theories. Journal of the Mechanics and Physics of Solids 59, 398–422. doi:https://doi.org/10.1016/j.jmps.2010.09.013.

Mazière, M., Forest, S., 2015. Strain gradient plasticity modeling and finite element simulation of Lüders band formation and propagation. Continuum Mechanics and Thermodynamics 27, 83–104. doi:DOI10.1007/s00161-013-0331-8.

McDowell, D.L., 2008. Viscoplasticity of heterogeneous metallic materials. Materials Science and Engineering: R: Reports 62, 67–123. doi:https://doi.org/10.1016/j.mser.2008.04.003.

Miehe, C., Schröder, J., Schotte, J., 1999. Computational homogenization analysis in finite plasticity simulation of texture development in polycrystalline materials. Computer Methods in Applied Mechanics and Engineering 171, 387–418. doi:https://doi.org/10.1016/S0045-7825(98)00218-7.

Nouailhas, D., Cailletaud, G., 1995. Tension-torsion behavior of single-crystal superalloys: Experiment and finite element analysis. International Journal of Plasticity 11, 451–470. doi:https://doi.org/10.1016/S0749-6419(98)80004-1.

Nye, J., 1953. Some geometrical relations in dislocated crystals. Acta Metallurgica 1, 153–162. doi:https://doi.org/10.1016/0001-6160(53)90054-6.

Panteghini, A., Bardella, L., 2018. On the role of higher-order conditions in distortion gradient plasticity. Journal of the Mechanics and Physics of Solids 118, 293–321. doi:https://doi.org/10.1016/j.jmps.2018.05.019.

Peerlings, R., Geers, M., de Borst, R., Brekelmans, W., 2001. A critical comparison of nonlocal and gradient-enhanced softening continua. International Journal of Solids and Structures 38, 7723–7746. doi:https://doi.org/10.1016/S0020-7683(01)00087-7.

Polizzotto, C., Borino, G., 1998. A thermodynamics-based formulation of gradient-dependent plasticity. European Journal of Mechanics - A/Solids 17, 741–761. doi:https://doi.org/10.1016/S0997-7538(98)80003-X.

Rice, J., 1971. Inelastic constitutive relations for solids: An internal-variable theory and its application to metal plasticity. Journal of the Mechanics and Physics of Solids 19, 433–455. doi:https://doi.org/10.1016/0022-5096(71)90010-X.

Ryś, M., Forest, S., Petryk, H., 2020. A micromorphic crystal plasticity model with the gradient-enhanced incremental hardening law. International Journal of Plasticity 128, 102655. doi:https://doi.org/10.1016/j.ijplas.2019.102655.

Scherer, J., Besson, J., Forest, S., Hure, J., Tanguy, B., 2019. Strain gradient crystal plasticity with evolving length scale: Application to voided irradiated materials. European Journal of Mechanics-A/Solids 77, 103768. doi:https://doi.org/10.1016/j.euromechsol.2019.04.003.

Scherer, J.M., Phalke, V., Besson, J., Forest, S., Hure, J., Tanguy, B., 2020. Lagrange multiplier based vs micromorphic gradient-enhanced rate-(in)dependent crystal plasticity modelling and simulation.

Computer Methods in Applied Mechanics and Engineering 372, 113426. doi:ttps://doi.org/10.1016/j.cma.2020.113426.

Steinmann, P., 1996. Views on multiplicative elastoplasticity and the continuum theory of dislocations. International Journal of Engineering Science 34, 1717–1735.

Steinmann, P., Stein, E., 1996. On the numerical treatment and analysis of finite deformation ductile single crystal plasticity. Computer Methods in Applied Mechanics and Engineering 129, 235–254. doi:https://doi.org/10.1016/0045-7825(95)00913-2.

Stölken, J., Evans, A., 1998. A microbend test method for measuring the plasticity length scale. Acta Materialia 46, 5109–5115. doi:https://doi.org/10.1016/S1359-6454(98)00153-0.

Teodosiu, C., Sidoroff, F., 1976. A theory of finite elastoviscoplasticity of single crystals. International Journal of Engineering Science 14, 165–176. doi:https://doi.org/10.1016/0020-7225(76)90085-9.

Willis, J., 1969. Some constitutive equations applicable to problems of large dynamic plastic deformation. Journal of the Mechanics and Physics of Solids 17, 359–369. doi:https://doi.org/10.1016/0022-5096(69)90023-4.

Wulfinghoff, S., Bayerschen, E., Böhlke, T., 2013. A gradient plasticity grain boundary yield theory. International Journal of Plasticity 51, 33–46. doi:https://doi.org/10.1016/j.ijplas.2013.07.001.

Wulfinghoff, S., Böhlke, T., 2012. Equivalent plastic strain gradient enhancement of single crystal plasticity: theory and numerics. Proc. R. Soc. A 468, 2682–2703. doi:https://doi.org/10.1098/rspa.2012.0073.

Wulfinghoff, S., Forest, S., Böhlke, T., 2015. Strain gradient plasticity modeling of the cyclic behavior of laminate microstructures. Journal of the Mechanics and Physics of Solids 79, 1–20. doi:https://doi.org/10.1016/j.jmps.2015.02.008.

Zhang, Y., Lorentz, E., Besson, J., 2018. Ductile damage modelling with locking-free regularised GTN model. International Journal for Numerical Methods in Engineering 113, 1871–1903. doi:https://doi.org/10.1002/nme.5722.